Age-associated Tissue Organisation Shifts Retinal Pigment Epithelium Actomyosin Plasticity in Phagocytosis

Teodora Piskova[1], Aleksandra N. Kozyrina[1], Giedrė Astrauskaitė[4], Mohamed Elsafi Mabrouk[3], Sebastian Schepl[1], Stacy Lok Sze Yam[1], Ragul Ravithas[1], Wolfgang Wagner[3], Massimo Vassalli[4] and Jacopo Di Russo[1,2]

[1]Institute of Molecular and Cellular Anatomy, RWTH Aachen University, Germany
[2]DWI-Leibniz-Institute for Interactive Materials, Aachen, Germany
[3]Institute of Stem Cell Biology, University Hospital of RWTH Aachen, Aachen, Germany
[4]Centre for the Cellular Microenvironment, James Watt School of Engineering, University of Glasgow, Glasgow, UK

Keywords: Postmitotic epithelium, RPE, Mechanical homeostasis, Ageing

Correspondence:

Jacopo Di Russo

jdirusso@ukaachen.de

Abstract

Mechanical homeostasis in healthy tissues relies on a dynamic balance of mechanical properties essential for maintaining tissue integrity and function. Over the lifetime, this integrity decays due to structural reorganisation from extracellular remodelling or an imbalance of cell death and proliferation. This is particularly challenging in postmitotic tissues such as the retina, where lack of proliferation requires age-dependent structural adaptation. The retinal pigment epithelium exemplifies this adaptation, compensating for apoptotic events through morphological reconfiguration and cytoskeletal remodelling. To explore the connection between age-related structural changes and mechanical homeostasis, we developed an *in vitro* model mimicking cell density reduction observed in the human retinal pigmented epithelium during ageing. This model is characterised by reduced cell height, shortened apical microvilli, and alterations in the actin cytoskeleton. The resulting age-associated phenotype leads to significant biomechanical changes, including tissue stiffening, enhanced junctional contractility, and apical cell cortex remodelling. Transcriptional profiling revealed notable shifts in actin-associated gene expression, suggesting potentially altered plasticity when actin remodelling is necessary, as for the phagocytosis of photoreceptor outer segments. Structurally aged monolayers exhibit changes in phagocytic activity that mirror those seen in aged individuals. Additionally, we observed an impaired capacity for apico-lateral remodelling during the internalisation of photoreceptor outer segments. This altered activity can be partially corrected by regulating actin network remodelling capacity with inhibitors targeting the actin nucleators ARP2/3 and formins. Overall, our findings suggest that age-related structural changes in the postmitotic retinal pigment epithelium shift its mechanical homeostasis, impacting physiological functions of the outer retina crucial for healthy vision.

INTRODUCTION

The structure and form of a biological entity determines its function, as described by the form-function paradigm (*1*, *2*). This paradigm applies across various length scales, from the molecular (*3*, *4*) and sub-cellular levels (*5*, *6*) to the tissue and organ levels, where proper architecture and cellular connectivity are essential for functionality (*7–9*). In recent decades, alongside form and organisation, increasing recognition as key parameters influencing function and homeostasis has also been given to the mechanical properties of tissues (*10–12*). These properties are determined by the cellular organisation and environment (*13–15*), and their maintenance within a preferred mechanical range for homeostasis is described by the principle of mechanical homeostasis (*16*). Mechanical homeostasis is particularly understudied in postmitotic tissues such as the central nervous system or the retina, which must adapt structurally to naturally occurring cell death to maintain the tissue's functional state (*17–20*).

An emblematic example of this adaptation are the age-related changes occurring in the retinal pigment epithelium (RPE) (*21*). In the retina, the RPE is located between the light-detecting photoreceptor cells and the choroid capillaries and provides vital metabolic support to photoreceptor cells (*22*). In ageing, this support is challenged by the steady rate of apoptosis in RPE (*23–25*), which needs to be actively compensated by the remaining cells, leading to major structural changes of the tissue. These include monolayer thinning, with the average RPE cell height reported to decrease (*26*). Furthermore, the RPE actin cytoskeleton remodels, leading to local fibres thickening or thinning with the formation of transcellular stress fibres (*27*). Finally, ageing has been shown to be associated with changes in RPE apical microvilli, which become shorter and sparser (*26*, *28*). In temporal correlation to these structural changes, the functional ability of the RPE to support photoreceptor cells changes towards a reduced ability to phagocyte and process photoreceptor outer segments (POS) fragments, with important implications for retinal degenerative pathologies (*29*, *30*).

While it has been proposed that the age-related changes in RPE organisation stem from a time-associated reduction in cell density, direct evidence supporting this hypothesis remains elusive. Moreover, the potential connection between these changes and a significant shift in the tissue's mechanical equilibrium, resulting in critical functional decline, remains a pressing and unresolved question.

To address these questions, we present an optimised *in vitro* experimental setup that induces large-scale apoptosis in mature RPE on demand, resulting in a significant reduction in cell density. This apoptosis-generated cell density (AgeD) recapitulates the structural RPE remodelling observed in ageing individuals. This includes a reduction in cell height, shortening of apical microvilli, and remodelling of the actin cytoskeleton. Moreover, AgeD in RPE is also associated with the altered POS fragments internalisation observed in ageing, characterised by the internalisation of lower fragment numbers and

a larger size of fragments. Finally, based on the RPE transcriptional profile, its biomechanical characterisation, and pharmacological modulation of actin nucleation, we suggest that this functional alteration results from a differential responsiveness of cortical actin during POS internalisation processes.

RESULTS

Apoptosis-generated cell density reduction *in vitro* phenocopies the structure of the ageing RPE

(*31*)Inspired by the natural reduction in cell density in RPE *in vivo* (*23*, *25*), we aimed to replicate age-associated cell loss *in vitro* by accelerating natural apoptosis to study the consequences of tissue adaptation during ageing.

Human induced pluripotent stem cell-derived RPE (iRPE) cells were cultured on 4 kPa soft polyacrylamide hydrogels with basement membrane-like coating as a reliable model for human RPE (*32–34*)(Sup. Fig. 1A). In these conditions, iRPE assumes a characteristic honeycomb-like organisation, apicobasal polarisation (Sup. Fig. 1B), and arrest of proliferation (0,01 to 0,41% within 24 h) (Fig. 1A and Sup. Fig.1C). To facilitate on-demand cell density reduction, on the 10th day of culture we transduced the cells with an adeno-associated virus (AAV) carrying a construct designed to promote the expression of FKBP-caspase 8 (Fig. 1B, Sup. Fig. 1D). FKBP-caspase 8 is pro-apoptotic fusion protein that can be activated on demand through AP20187-induced dimerization, initiating the cellular suicide program (*35*). Therefore, after reaching a stable expression, on the 15th day, we incubated the monolayer with the compound AP20187, inducing monolayer-scale apoptosis that led to the extrusion of 2% of the cells within the observation time (Fig. 1B-C, Sup. Fig. 1E and Video 1). By the 20th day (96 hours after apoptosis completion), the iRPE monolayer showed a reduction of cell density of approximately 8% (Fig. 1D), which was not compensated by increased proliferation. In fact, we quantified significantly lower proliferation rates compared to control monolayers (Fig. 1A). As a result, the obtained monolayer was referred to as apoptosis-generated cell density (AgeD) in iRPE or AgeD-iRPE.

Morphologically, AgeD-iRPE presents cells with a larger area on average (Fig. 1E, Sup. Fig. 1F and G) without experiencing any fluidification or unjamming, as evident by cellular area distribution and shape factor (Sup. Fig. 1H and I), recapitulating morphological changes observed in human RPE ageing (*24*). Furthermore, we noticed that one-tenth of cells within AgeD-iRPE presented transcellular stress fibres (Fig. 1F), which were also reported to occur frequently in human RPE ageing (*27*). Next, we quantified the cell height in fixed and mounted samples (Fig. 1G and H), showing that AgeD-iRPE is significantly thinner than the controls (9.1 vs 11.6 µm), in agreement with previous results for the ageing RPE (*26*, *36*). Lastly, motivated by the documented changes of microvilli size and number in the ageing RPE (*26*, *28*), we evaluated ezrin as a polarity marker and microvilli

organiser (*37–39*). Qualitative analyses of ezrin staining revealed a distinct morphology of the cellular apices between AgeD-iRPE and control (Fig. 1I), which can also be quantitatively captured by the reduced protein level detected in the cells by western blot (Fig. 1J). Moreover, the examination of the microvilli length by confocal microscopy showed approximately one-third shorter microvilli in the AgeD-iRPE compared to the control (Fig. 1K). Based on the studies performed on Ezrin$^{-/-}$ mice (*37*), these observed differences strongly suggest that in the AgeD conditions, the microvilli are less elaborated and more disorganised. Finally, the quantification of the active form of ezrin (phosphorylated ezrin), which connects the actin cortex to the membrane (*40*), revealed a significant decrease in the AgeD condition (Fig. 1L).

To exclude the influence of the viral delivery on the observed age-mimicking restructuring, we included a matched viral control, which promoted the expression of GFP (GFP-iRPE) (Sup. Fig. 2A). Compared to this control, the AgeD-iRPE was still showing a reduced cell density and cell height (Sup. Fig. 2B, C and D), as well as significant differences in both organisation and length of ezrin-positive microvilli (Sup. Fig. 2E). Next, we addressed the observation that despite most of the cells within the monolayer expressed the reporter after transduction, only a few of the cells ultimately underwent apoptosis during the AP20187 treatment (Video 1). To exclude any possible effects of the leftover recombinant protein in the remaining cells, we included an additional 'mixed' control in the analyses consisting of an iRPE monolayer made by a mixed population of transduced (10%) and naïve cells. This condition allowed us to target the caspase activation only on a subpopulation of cells (Sup. Fig. 2F and G). Interestingly, with this approach, apoptosis still caused a significant cell density and height reduction, confirming that these features are independent of the possible presence of inactive recombinant protein in the cells (Sup. Fig. 2H and I). Lastly, we asked whether the changes were induced by secondary factors released in the medium after the large-scale apoptosis induction (*41*). Hence, we transferred a medium pre-conditioned by the AgeD-iRPE sample during and after apoptosis onto control monolayers (Sup. Fig. 2J). Nonetheless, the quantification still showed no effect of the "conditioned medium" on cell morphology, density, or height (Sup. Fig. 2K, L and M).

Altogether, we present an *in vitro* model based on cell density reduction via on-demand apoptosis that phenocopies key morphological features of the aged RPE. These features include lower cell density, the presence of transcellular actin fibres, reduced cell height, and shorter and remodelled microvilli.

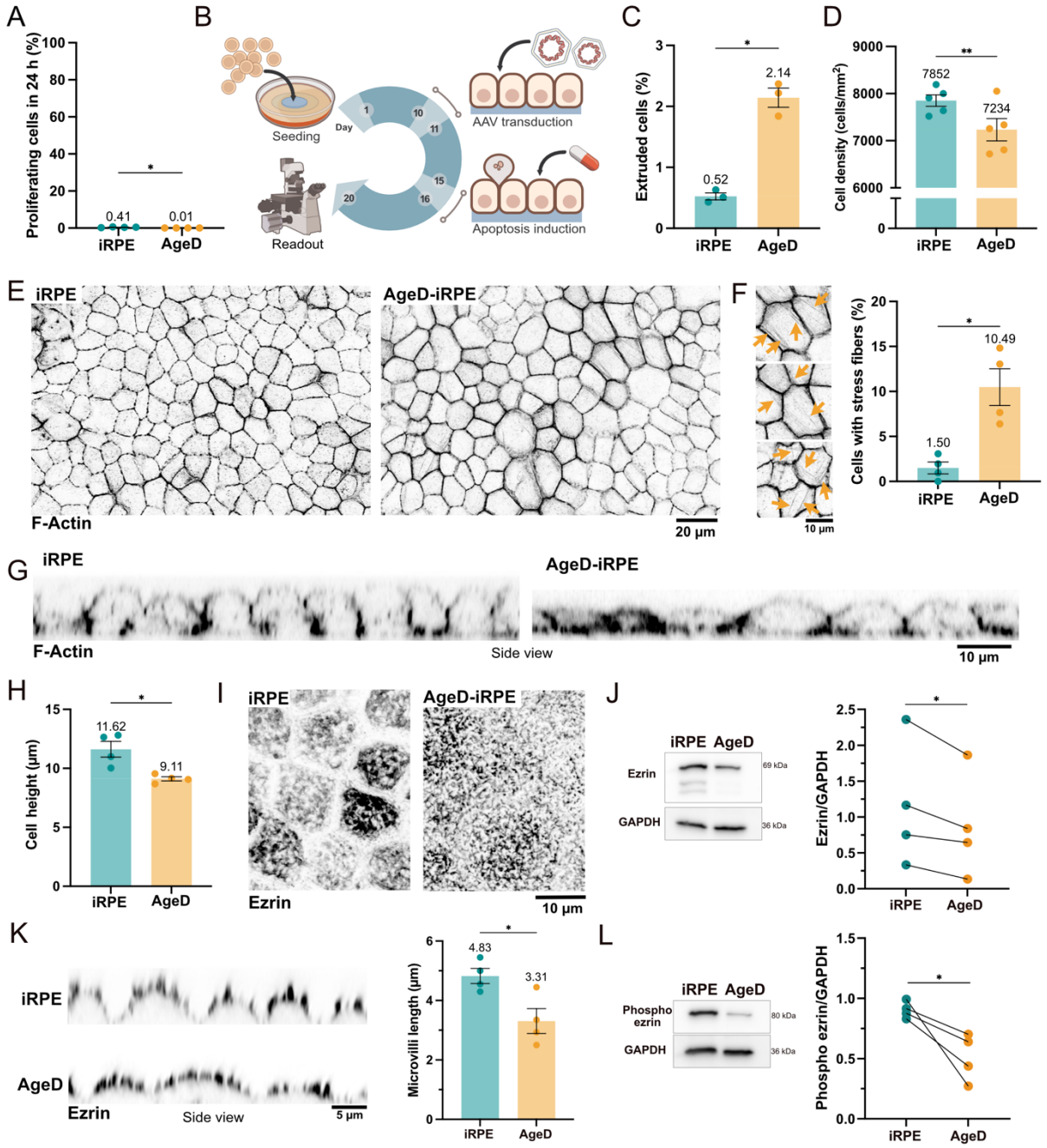

Figure 1: AgeD in iRPE recapitulates key structural features of aged RPE. A: Quantification of proliferating cells within the monolayers on day 20. **B:** Experimental timeline highlights key steps of the experiment, including cell seeding on hydrogels (day 1), AAV-mediated transduction with FKBP-casp8-encoding plasmid (day 10 to 11), apoptosis induction by the addition of the dimerising drug AP20187 (day 15 to 16), and day of read-out (day 20). **C:** Quantification of extruded cells during the apoptosis induction. **D:** Quantification of cell density within the monolayers on day 20. **E:** Representative optical sections of iRPE and AgeD-iRPE stained for F-actin, which reveals cell organisation and sizes. **F:** Zoomed-in images from the AgeD-iRPE with arrows indicating the local presence of transcellular stress fibres (left). Quantification of cells with transcellular fibres (right). **G:** Orthogonal cross-sections of F-Actin micrographs. **H:** Quantification of cell height. **I:** Monolayer apical signal of ezrin highlighting microvilli organisation. **J:** Immunoblots showing ezrin and GAPDH as a housekeeping protein (left) and quantification of total ezrin protein from immunoblots, normalised to GAPDH (right). Paired values from the same experiment are connected with lines. **K:** Representative orthogonal views of iRPE monolayers stained for ezrin showing the apical microvilli (left) and the quantification of their average length (right). **L:** Immunoblots showing phosphorylated ezrin and GAPDH as a housekeeping protein (left) and their quantification (right). Paired values from the same experiment are connected with lines. Datapoints represent average values per experiment (± SEM in case of bar graphs) originating from 3 to 5 independent experiments. Statistical significance in A, C, D, F, H and K was tested using a paired t-test, where *: $p<0.05$, **: $p<0.01$. Statistical significance in J and L was tested using a ratio paired t-test, where *: $p<0.05$.

Impaired internalisation of photoreceptor outer segment fragments in AgeD-RPE

One of RPE's main functions *in vivo* is the daily engulfment and internalisation of oxidised fragments of photoreceptor outer segments (POS), often referred to in the literature as POS phagocytosis (*42*) or, due to the active nature of nibbling involved, as trogocytosis (*43*). During ageing, the ability of RPE to phagocytose and process POS fragments declines with important implications for the co-occurrence of retinal degenerative pathologies (*29*, *30*). Hence, we asked whether the reduction of cell density in RPE alone can impair their ability to internalise POS. Thus, following an established assay (*34*, *44*), we incubated control and AgeD-iRPE with fluorescently labelled porcine POS fragments in the presence of bridging molecules Protein-S and MFG-E8 for 4 h (Fig. 2A). During this time, some of the fragments bound to the apical surface of the iRPE and some got internalised by the cells (Fig. 2A and B). After 3D segmentation, we used the apical actin signal to differentiate between bound and internalised fragments (Sup. Fig. 3A). Quantification revealed that the AgeD-iRPE exhibited significantly fewer internalised particles, both within the field of view or when normalised by cell number (Fig. 2C, Sup. Fig. 3B). Next, motivated by a reported trend of larger POS phagosomes in the RPE of aged animals (*45*), we further quantified the volume of the internalised photoreceptor fragments. Surprisingly, we found the average volume of internalised fragments to be larger in AgeD-iRPE monolayers (Fig. 2B and D). Regarding the bound particles, neither their number, nor their average volume was found to be significantly different (Sup. Fig. 3C). Similar differences in internalised particle number and volume were observed in the mixed cell population subjected to cell density reduction, with fewer internalised particles and a larger average particle volume (Sup. Fig. 3E, G). Finally, the medium transfer from the apoptotic induced samples showed no significant impact on either the internalised particles count or on the fragment volume (Sup. Fig. 3F and H).

Altogether, these data demonstrate that AgeD-iRPE monolayers exhibit deficient internalisation of POS fragments, internalising fewer and larger fragments.

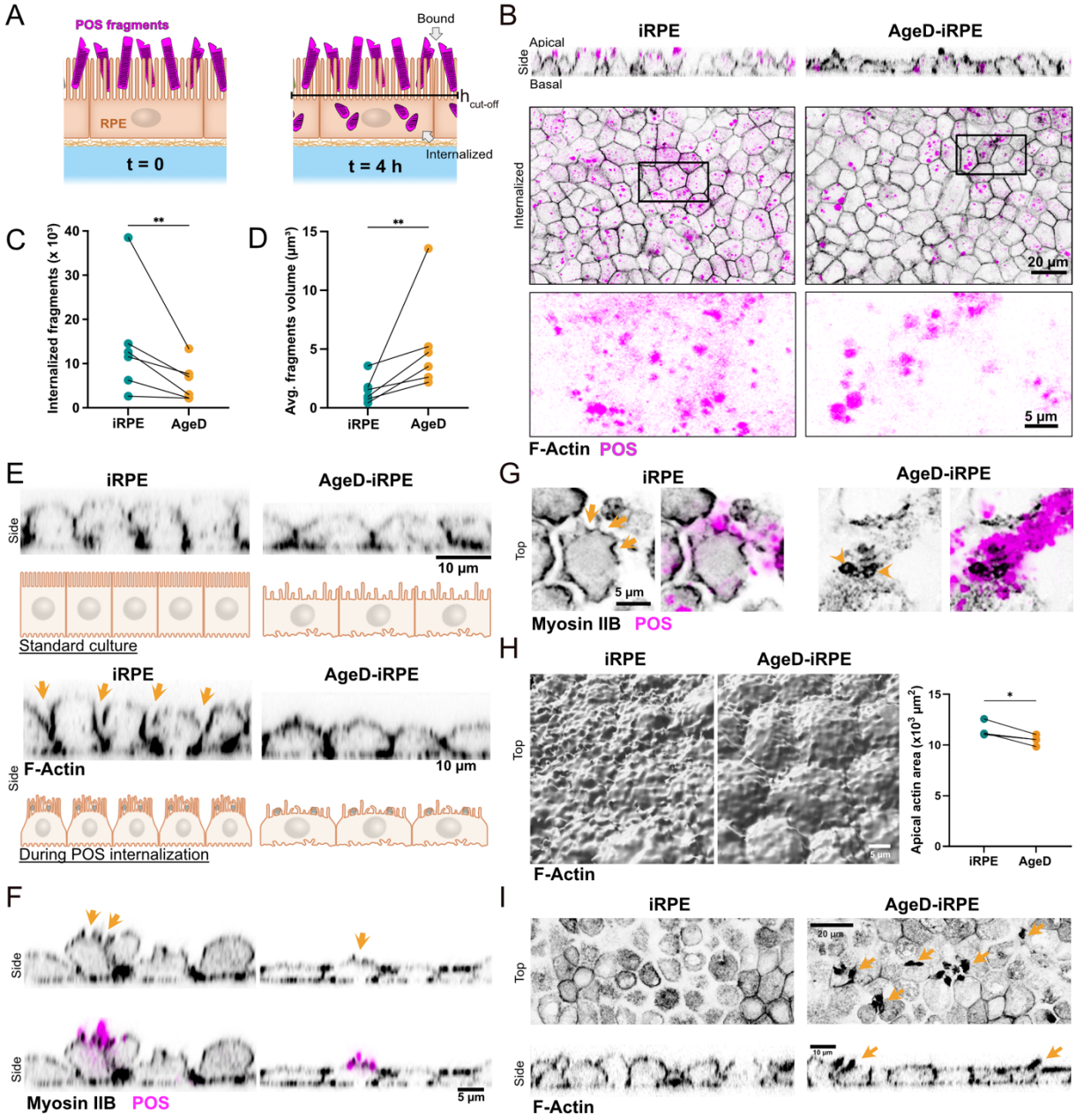

Figure 2: AgeD-iRPE shows altered internalisation of POS fragments. A: Schematics of POS fragment internalisation assay. Isolated and labelled porcine POS fragments are fed to iRPE together with bridging molecules at timepoint 0 and analysed four hours later. To distinguish between bound and internalised fragments, we define a cut-off height. **B:** Representative orthogonal cross-sections and single optical slices of iRPE and AgeD-iRPE at t = 4 h. Zoom-in of the POS signal from the inlet showcases the size of the fragments. **C:** Quantification of fragments internalised within the time of the assay. Values are shown as times thousand per field of view. **D:** Quantification of the average volume of internalised fragments. Data points represent average values per experiment originating from 6 independent experiments. Statistical significance was tested using a ratio paired t-test, where **: $p<0.01$. **E:** Representative orthogonal cross-sections of F-actin labelled monolayers in a standard culture condition vs during the POS internalisation assay. Images are not paired. Schematic illustration and arrows highlight the distinct cross-sectional morphology of cells, with control cell bodies bulging out above the level of cell-cell junctions. **F:** Representative orthogonal cross-sections of Myosin IIB labelled monolayers and FITC-labelled POS fragments. Myosin IIB is enriched in proximity to the POS (arrows). **G:** Representative apical view of iRPE cells in control and AgeD condition, stained for Myosin IIB during internalisation of POS-FITC. In contrast to many small phagocytic cups localised apically and laterally in iRPE (arrows), AgeD-iRPE shows fewer apical-only cup-like structures with more localised myosin signal (arrowheads). **H:** Representative 3D segmentation of apical F-actin surface of monolayers during internalisation assay (left) and quantification of apical actin area within the same field of view (right). Datapoints represent average values per experiment originating from 3 independent experiments. Statistical significance was tested using a ratio paired t-

test, where *: p<0.05. **I**: Representative apical and orthogonal cross sections of monolayers during internalisation. Arrows indicate the presence of protruding actin-rich structures in AgeD-iRPE.

Altered actomyosin plasticity and mechanical properties in AgeD-iRPE

POS phagocytosis relies on the active remodelling of the apical actin network, which plays a crucial role in fragment internalisation and phagosome size (*34*, *43*, *44*). Actin dynamics are essential throughout the process, guiding key steps from initial binding and ensheathment to the final scission of the phagosome (*42*, *46*). Thus, we examined the morphology of the apical actin during internalisation, on a few-cell scale in our 3D segmentation and on a larger monolayer scale. In the side view, we noticed the apical actin of control iRPE monolayers experienced a substantial deformation during the internalisation, such as bulging and enlargement of the protruding cell portion above the cell junctions and clear formation of myosin IIB-positive cups (Fig. 2E-H). In contrast, AgeD-iRPE did not experience much evident deformation, and phagocytotic cups were less resolved (Fig. 2F and G). Next, we noticed that cells in the AgeD condition displayed a different apical actin topography compared to the control, having an overall smoother surface, as quantified by area per field of view (Fig. 2H). Finally, on the monolayer scale, we noticed that the AgeD-iRPE frequently presented large actomyosin-rich apical structures (Fig. 2G and I, Sup. Fig. 4), which were absent in iRPE samples.

These observations suggest that iRPE cells in the AgeD condition exhibit altered plasticity in remodelling their actomyosin cytoskeleton when internalising POS fragments. Consequently, we wondered whether the differences stemmed from distinct patterns of actin-cytoskeleton-related signalling. Hence, we examined the myocardin-related transcription factor A (MRTFA), which is known to regulate actin-associated signalling (*47*). We observed a short-term translocation of MRTFA into the nucleus at day 17, shortly after the large-scale cell loss, which went back to levels comparable to the control at day 20, or the day of the read-out (Fig. 3A and B). This demonstrates that the AgeD condition is reached by a transient transcriptional adaptation, possibly conveying the observed structural remodelling. We then examined the mRNA expression of actin-associated proteins after bulk RNA sequencing (Fig. 3C, Sup. Fig. 5A). Examining more precisely the expression of these proteins showed an array of significantly differentially expressed actin-related genes in the AgeD condition. Upregulated genes in AgeD-iRPE contained genes related to actin branching, polymerisation, depolymerisation, and crosslinking (*ARPC2, PFN1, FHOD3, INF2, CFL2, ACTN1, FSCN1, FLNA*). Downregulated genes included ezrin and the formins *DIAPH1, DIAPH2, DAAM1* and *DAAM2* (Fig. 3D and E). Moreover, we aimed to compare the overall gene expression changes between iRPE and AgeD-iRPE with those reported in ageing RPE from two independent studies (*48*, *49*) (Sup. Fig. 5 B-D). Considering the significant differences from our reductionist approach and *in vivo* human data, as well as the differences between the results of the studies, it is worth noting that our model may mimic further aspects of RPE ageing besides the actomyosin remodelling discussed in this work.

Altogether, these insights point to a different fingerprint of actin-associated proteins in the AgeD-iRPE, which may lead to an altered capacity to remodel in response to phagocytosis stimulation.

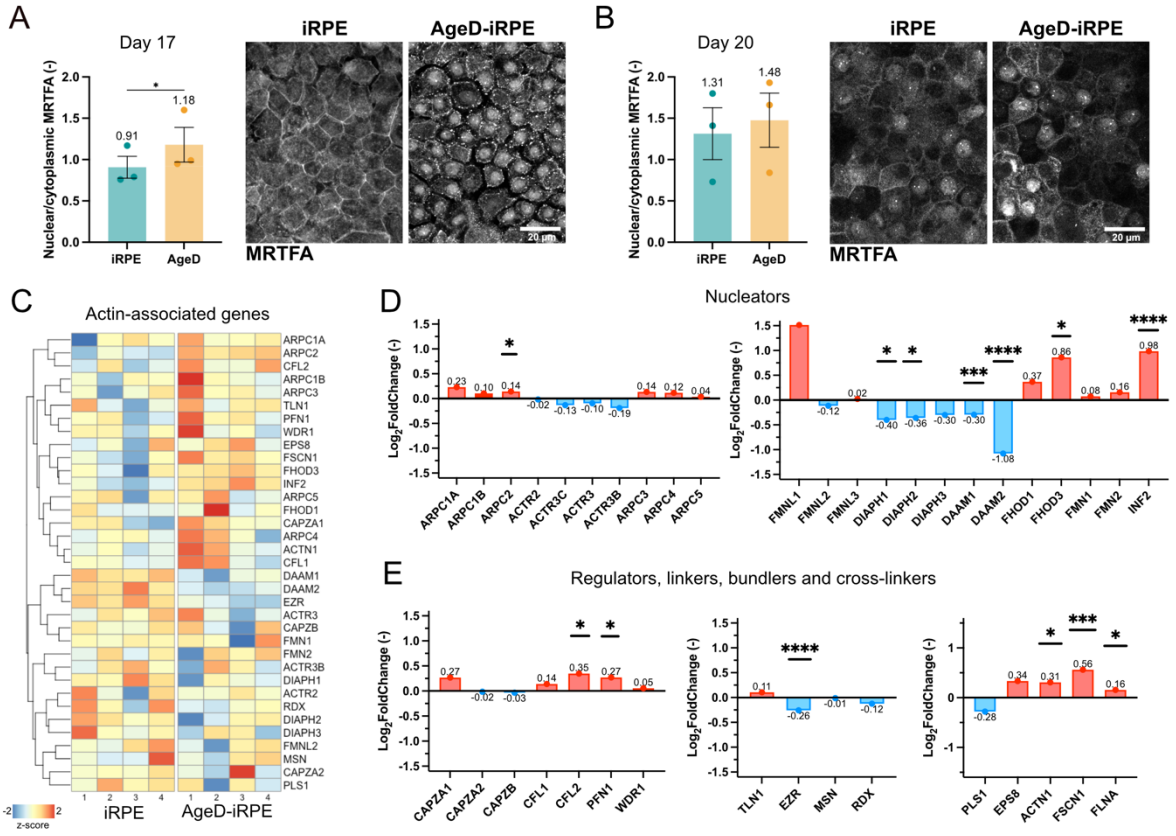

Figure 3: A different fingerprint of cortical actin and actin-associated proteins in AgeD-iRPE. A: Quantification of nuclear to cytoplasmic MRTFA fluorescence intensities and representative micrographs of MRTFA staining one day after apoptosis induction (day 17). **B:** Quantification of MRTFA fluorescence intensities and representative micrographs of MRTFA staining on the day of readout (day 20). Datapoints in A and B represent average values per experiment ± SEM originating from 3 independent experiments. Statistical significance was tested using a ratio paired t-test, where *: $p<0.05$. **C:** Hierarchically clustered heatmap of RNA transcript counts of actin-related proteins from four experiments of iRPE vs AgeD-iRPE samples. **D:** Graphs showing the Log2Fold change in RNA transcript expression of branched (left) and linear (right) actin nucleator proteins for AgeD-iRPE vs. iRPE. **E:** Graphs showing the Log2Fold change in RNA transcript expression of actin assembly/disassembly regulators (left), actin membrane linkers (middle) and crosslinkers and bundlers (right) for AgeD-iRPE vs. iRPE. Differentially expressed genes in D and E are marked with *: $p_{adj}<0.1$, **: $p_{adj}<0.01$, ***: $p_{adj}<0.001$, and ****: $p_{adj}<0.0001$ as a result of the use of negative binomial generalised linear models and Wald test.

As RPE mechanics has been associated with phagocytotic activity (*34*), we sought to determine whether the observed actin network remodelling would affect the mechanical properties of AgeD-iRPE. To characterise the viscoelastic properties of the monolayer as a multicellular system, we conducted nanoindentation using a spherical tip with a diameter of 20 µm, allowing to probe a contact area of approximately 10 µm in diameter (Fig. 4A, Sup. Fig. 6A, Video 2). This approach allowed us to measure the Effective Young's modulus of the uppermost 2.5 µm of the monolayer, which approximately corresponds to the apical-most 9% of the cell height (average height of live iRPE is 27.8 ± 0.6 µm). The Effective Young's modulus of AgeD-iRPE was roughly one-third higher (694 Pa vs 513 Pa), pointing to a stiffer tissue (Fig. 4B). Next, using the same nanoindentation setup, we quantified both storage and loss moduli at different probing frequencies to characterise

244 the monolayer viscoelasticity (*50*). Unexpectedly, we found significant increase in the
245 storage modulus of the AgeD-iRPE while the loss modulus remained unchanged (Fig. 4C,
246 Sup. Fig. 6B). Similar differences were observed when AgeD-iRPE was compared to the
247 virus control or when the condition with mixed cell population was analysed without or
248 with cell extrusion (Sup. Fig 6D and E). In the latter case, the differences in stiffness and
249 storage modulus were smaller and only apparent at the lower probed frequencies (1 and
250 2 Hz). Lastly, medium transfer controls seemed to experience softening rather than
251 stiffening, excluding an effect of apoptotic debris on the observed stiffening in AgeD-iRPE
252 (Sup. Fig. 6F).

253 As mechanical properties and contractility are often linked (*51*, *52*), we examined the
254 levels of phosphorylated myosin light chain 2 (pMLC2) to obtain a general idea about
255 actomyosin contractility (*53*) . Immunoblotting revealed general increased levels of
256 pMLC2 in the AgeD condition (Sup. Fig. 6C), pointing to overall higher actomyosin
257 contractility, especially localised at the cell-cell junctions as shown by
258 immunofluorescent staining (Fig. 4D and D^{I}). This observation was further supported by
259 enrichment of vinculin at the cell-cell and at the tricellular junctions (Fig. 4E and E^{I}),
260 pointing to higher contractile force at cell-cell junctions (*54*).

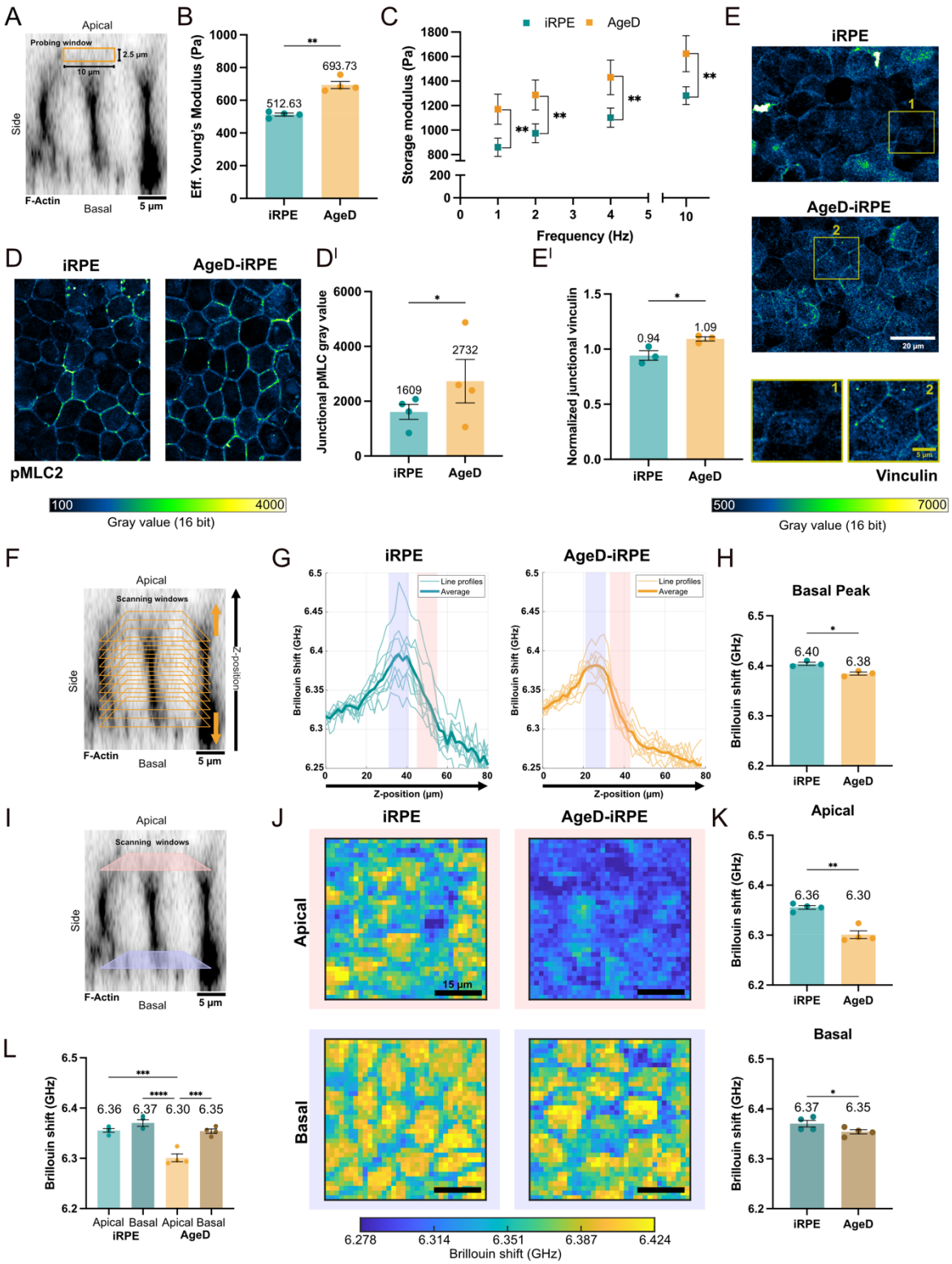

Figure 4: AgeD-iRPE presents a new biomechanical state. A: Image illustrating the probing window (10 x 2.5 µm) during nanoindentation on an orthogonal cross-section of F-Actin-labelled live iRPE. **B:** Average Effective Young's Modulus measured by nanoindentation scans in iRPE and AgeD-iRPE. **C:** Average storage modulus at different oscillation frequencies. **D:** Representative images of pMLC2-labelled iRPE monolayers with grey values represented in the colour bar. **D'**: Quantification of junctional pMLC2 signal. **E:** Representative images of vinculin-labelled iRPE monolayers with annotated regions enlarged. **E'**: Quantification of junctional fluorescence signal of vinculin normalised to cytoplasmic fluorescence signal. **F:** Image illustrating the geometry of low-resolution Brillouin z-scans on an orthogonal cross-section of F-Actin-labelled live iRPE. **G:** Representative line profiles of the z scans showing the Brillouin shift values starting from the hydrogel, across the iRPE monolayers and reaching into the cell medium. Averages of z-scans are represented with thicker lines. Highlighted in light lilac and salmon are the approximate basal

and apical cell regions, respectively. **H:** Quantification of Brillouin shift values obtained by fitting the peaks of the curves shown in **G**. **I:** Image illustrating high-resolution 2D raster scan windows on an orthogonal cross-section of F-Actin-labelled live iRPE. **J:** Representative Brillouin shift maps obtained from the 50 x 50 µm apical and basal scans of the iRPE monolayers. **K:** Quantification of mean Brillouin shift values from 50 x 50 µm regions of interest recorded in apical and basal regions in iRPE monolayers. **L**: Comparative bar plot of apical and basal Brillouin shifts in iRPE and AgeD-iRPE cells. Data points represent average values per experiment ± SEM originating from 3 to 4 independent experiments. Statistical significance in **B** and **C** was tested using a paired t test, in **D**^{I} and **E**^{I} – using a ratio paired t test, where *: $p<0.05$, **: $p<0.01$, ***: $p<0.001$ and ****: $p<0.0001$. Statistical significance in **H** and **K** was tested using a paired t-test, and in **L** using a one-way ANOVA, where *: $p<0.05$, **: $p<0.01$, ***: $p<0.001$, and ****: $p<0.0001$.

Nanoindentation enabled us to characterise the biomechanical properties of the RPE from the apical side. Our indentation setup was designed to probe multicellular length scale deformation, where the indentation of the 20 µm tip at the selected depth is counteracted by intercellular junctions (*55*) (Fig. 4A, Sup. Fig. 6A, Video 2). To characterise subcellular mechanical properties of the RPE monolayer non-invasively, i.e., independently from intercellular adhesion, we applied Brillouin micro-spectroscopy. Here, the detection of photons, inelastically scattered by thermally-induced acoustic phonons, enables the probing of viscoelastic properties within the sample at microscale resolution (*56*). Using Brillouin microscopy, we first performed low-resolution z-scans through iRPE and AgeD-iRPE monolayers, including the surrounding hydrogel and medium (Fig. 4F). These line profiles revealed the presence of a peak in the Brillouin shift, corresponding to the cellular basal side, which gradually decreased towards the apical cell region (Fig. 4G). The quantification of fitted peak values of these line profiles revealed significantly lower Brillouin shift in AgeD-iRPE compared to iRPE (Fig. 4H). Moreover, based on the peaks shown in Figure 4G and confirmed by live-cell brightfield imaging, we identified the apical and basal z-levels for conducting 2D high resolution raster scans (Fig. 4I). The 2D raster scans (50 x 50 µm) revealed mechanical compartmentalisation into areas with different Brillouin shifts, which may correspond to cellular and intercellular regions (Fig. 4J). Notably, this compartmentalisation was much more evident at the basal sides. The quantification of the mean Brillouin shifts revealed a difference between the conditions, with AgeD-iRPE cells showing lower average values at the apical (6.30 vs 6.36 GHz) and basal (6.35 vs 6.37 GHz) sides of the cells (Fig. 4K). Interestingly, when comparing apical and basal shifts within the same conditions, AgeD-iRPE cells showed significantly different apical shifts compared to basal, which was not the case in iRPE (Fig. 4L). Overall, this supports the idea that the apical sides of the cells undergo the most pronounced reorganisation in AgeD-iRPE.

To exclude the influence of intercellular junctions on the average shift values, we aimed to separate the shifts of “cell edges" from those of "cell bodies". As this distinction was not clear in the apical scans, we performed the analysis on the basal sides, where the distribution of shift values revealed two distinct modes (Sup. Fig. 7A and B). Quantification based on segmented Brillouin shift plots shows that, regardless of the experimental condition, the interstitial regions of the monolayer (“cell edges”) consistently exhibit lower shifts than the cell cores (“cell bodies”). This also confirms a trend toward reduced core shifts in AgeD-iRPE (Sup. Fig. 7C and D). Notably, the lower shift in the interstitium across both conditions likely reflects the absence of well-defined

316 intercellular junctions at the basal side, and instead, the presence of loosely
317 interdigitated basal membranes, as seen in F-actin staining (Sup. Fig.7E).

318 Altogether, biomechanical characterisation at the two different length scales showed
319 that the age-associated RPE phenotype has a different biomechanical state of the tissue.
320 This mechanical state includes higher contractility at the apical intercellular junctions,
321 which confers a stiffer and more elastic tissue, as evident by the nanoindentation. At the
322 subcellular level, this trend is opposite, as a lower Brillouin shift suggests a softer cell
323 apex.

324 **Modulating cortical actin remodelling differentially impacts POS phagocytosis**

325 Motivated by our observations on cortical actin topography, mechanics, and the
326 differential expression of actin-related regulators, we aimed to directly investigate the
327 cause-effect relationship between POS internalisation and actin remodelling. To this
328 end, we targeted actin nucleation, a key process influencing cortical thickness and
329 membrane tension (*57*). For the experimental design, we considered the upregulation of
330 ARP2/3 subunit mRNA expression and the downregulation of several formins in AgeD-
331 iRPE (Fig. 3D), along with the distinct actin structures observed during internalisation.
332 AgeD-iRPE exhibited a larger, flatter actin surface topography (Fig. 2I and L), suggesting
333 an abundance of heavily branched actin, similar to that found in lamellipodia. In contrast,
334 control samples displayed more numerous, smaller, and protruding actin structures (Fig.
335 2I and L), resembling filopodia, which are characterised by linear actin cores and highly
336 dependent on formin activity (*58*). Based on these findings, we inhibited ARP2/3 activity
337 in AgeD-iRPE using the compound CK-666(*59*) and inhibited formins activity in the control
338 iRPE using the compound SMIFH2 (*60*).

339 Formins inhibition in iRPE did not affect their height but significantly stiffened the
340 monolayer on a tissue level (Sup. Fig. 8A, B). When tested for the POS fragments
341 internalisation, the quantification showed a highly variable effect on the number of
342 internalised particles, with no conclusively significant impact for both internalised and
343 bound POS fragments (Fig. 5A and B; Sup. Fig. 8C and D). Nonetheless, the fragments'
344 size was significantly affected by SMIFH2, leading to larger fragments on average (Fig. 5A
345 and B). Moreover, during internalisation, the 3D-segmented actin had a smoother
346 topography, which, however, was not captured by the quantification of the total apical
347 actin area (Fig. 5C; Sup. Fig. 8E). Finally, when observed orthogonally, formins-inhibited
348 iRPE also bulged out upwards similarly to control monolayers but showed denser F-actin
349 signal at the junction, suggesting a later reinforcement similar to AgeD-iRPE (Fig. 5D).
350 Moreover, the bulging cells showed a more irregular apical morphology (Fig. 5D).

351 The inhibition of ARP2/3 using CK-666 in AgeD-iRPE led to a slightly increased cell height
352 (Sup. Fig. 8F), but no significant changes in monolayer stiffness (Sup. Fig. 8G). During
353 phagocytosis, treated AgeD-iRPE internalised an increased number of particles (Fig. 5E
354 and F; Sup. Fig. 8H), while the average internalised particle size and the number of bound

355 particles remained comparable (Fig. 5E, G, Sup. Fig. 8H and I). Morphologically, the 3D-
356 segmented cortical actin during internalisation showed the occasional presence of
357 thinner and longer ruffles (Fig. 5G), which resulted in a significant increase in the
358 quantified apical actin area (Sup. Fig. 8J). Furthermore, orthogonally, the treated AgeD-
359 iRPE showed some degree of 'bulging' during phagocytosis, which was more noticeable
360 compared to the untreated AgeD-iRPE (Fig. 5H).

361 Overall, these results demonstrate that modulating actin cytoskeleton remodelling by
362 interfering with actin nucleation effectively altered cortical actin responsiveness during
363 internalisation. These manipulations were sufficient to replicate differences in
364 photoreceptor internalisation observed in AgeD-iRPE. Particularly, ARP2/3 activity
365 appears to be related to cell 'budging', modulating apical actin area and cell height,
366 which impacts the number of internalised particles, while formins activity modulates
367 tissue-level stiffness, impacting the size of the internalised particles.

368 These insights strongly suggest that AgeD-iRPE establishes a new mechanical
369 equilibrium and homeostasis, resulting in reduced actin-myosin network plasticity
370 necessary for POS internalisation (Fig. 6).

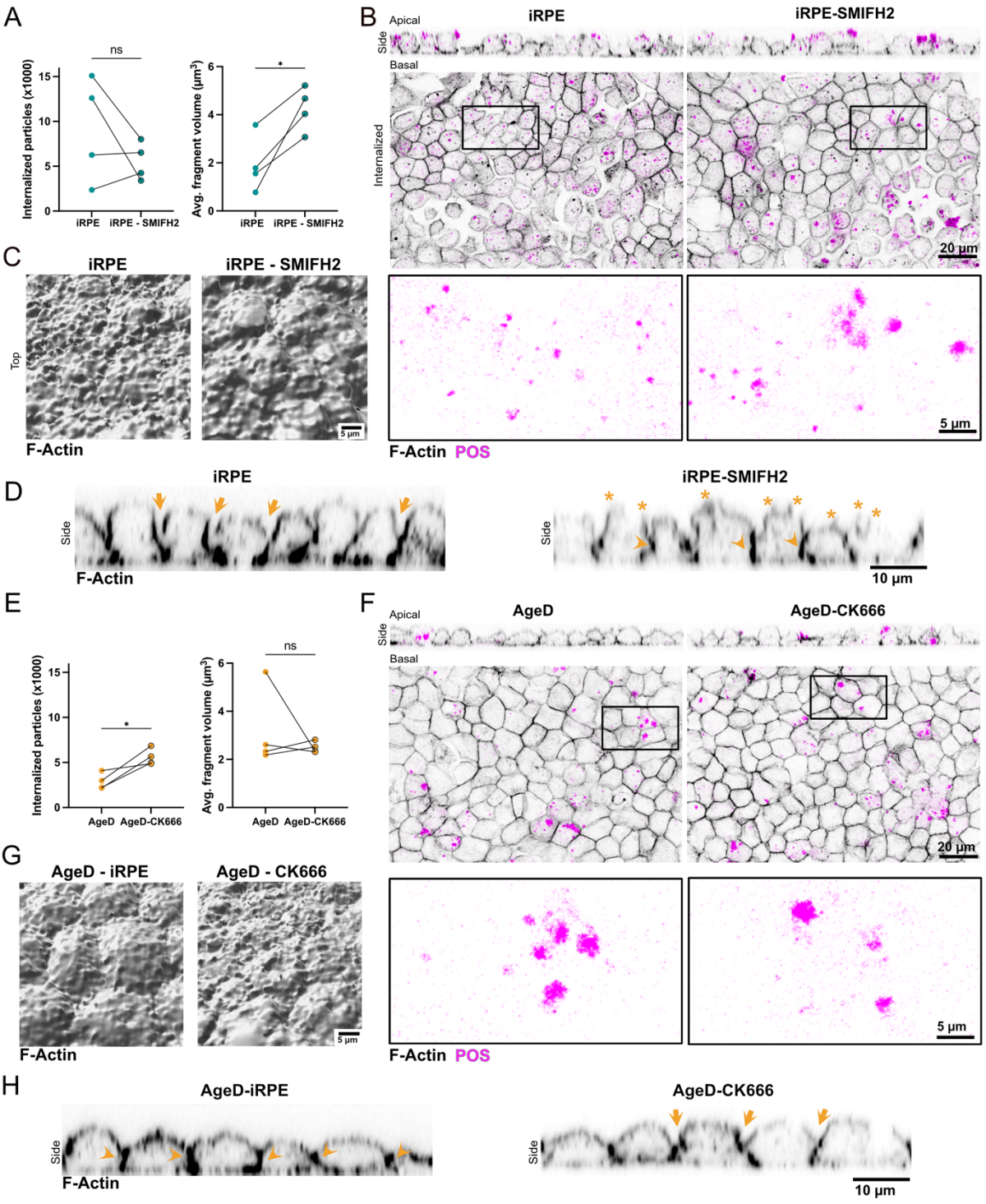

Figure 5: Actin cortex modulation via nucleator inhibitors affects POS internalisation process. A: Number of internalised fragments (left) and their average volume (right) for iRPE vs iRPE treated with 20 µM SMIFH2. **B:** Representative orthogonal cross-sections and single optical slices of iRPE and SMIFH2-treated iRPE at t = 4 h. Zoom-in of the POS signal from the inlet showcases the size of the fragments. **C:** Representative 3D segmented apical F-actin surface of monolayers during POS internalisation assay for iRPE vs SMIFH2-treated iRPE. **D:** Representative orthogonal cross-sections of F-actin labelled monolayers during POS internalisation assay of untreated and SMIFH2-treated iRPE. Arrows indicate the junctional remodelling to induce cell bulging, arrowheads indicate the junctional reinforcement, and stars highlight apical irregularities. **E:** Number of internalised fragments (left) and their average volume (right) for AgeD-iRPE vs AgeD-iRPE treated with 500 nM CK-666. **F:** Representative orthogonal cross-sections and single optical slices of AgeD-iRPE and CK666-treated AgeD-iRPE at t = 4 h. Zoom-in of the POS signal from the inlet showcases the size of the fragments **G:** 3D segmented apical F-actin surface of monolayers during POS internalisation assay for untreated vs CK666-treated AgeD-iRPE. **H:** Representative orthogonal cross-sections of F-actin labelled monolayers during photoreceptor fragment internalisation assay of untreated and CK666-treated AgeD-iRPE. Arrows indicate the junctional remodelling to induce cell bulging, while arrowheads indicate the junctional reinforcement. Datapoints

386 represent average values per experiment originating from 4 independent experiments. Statistical significance was
387 tested using a ratio paired t-test, where *: p<0.05.

388 DISCUSSION

389 In this work, we present a first-of-a-kind model of structural ageing for the RPE that
390 isolates the structural aspect of tissue ageing from other hallmarks of ageing (*61*, *62*). The
391 model is inspired by the natural loss of cells through apoptosis within the postmitotic RPE
392 monolayer. Comparing AgeD-iRPE with iRPE, we demonstrate significant changes in
393 biomechanical features that evidence a shift in RPE mechanical homeostasis related to
394 structural ageing. Most importantly, this shift has implications for the function of POS
395 internalisation, potentially leading to impaired tissue performance. We identify
396 remodelling of the actin cytoskeleton as a key factor mediating both the structural tissue
397 adaptation to cell loss and the observed functional differences, suggesting that tissue
398 preservation may be prioritised at the expense of functional trade-offs in ageing RPE.
399 Ultimately, this structural adaptation significantly alters the actomyosin plasticity
400 necessary for POS phagocytosis (Fig. 6).

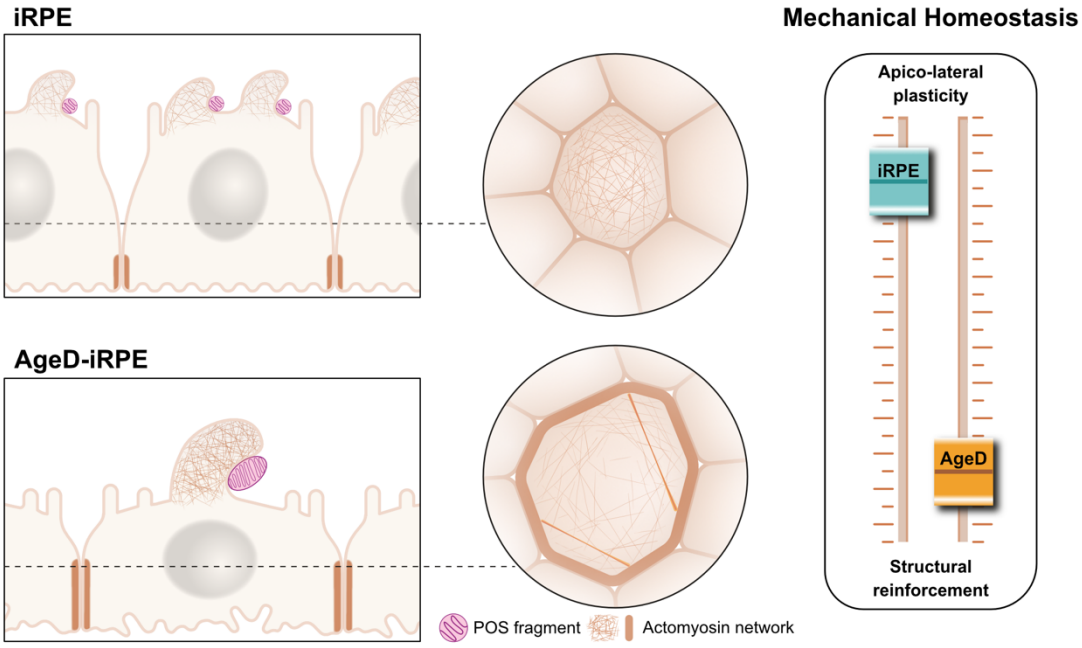

401

402 **Figure 6: Apoptosis-generated density reduction leads to a shift in RPE mechanical homeostasis.** The density
403 reduction in iRPE due to apoptosis mimics structural features of aged RPE, revealing biomechanical alterations that
404 indicate a shift in mechanical homeostasis. These changes correlate with a reduced number of internalised POS
405 fragments, which are larger in size, highlighting functional decline. Actin cytoskeleton remodelling mediates structural
406 reinforcement and functional alteration, suggesting a trade-off where tissue structural preservation compromises the
407 apico-lateral plasticity essential for POS phagocytosis.

408 Ageing is a multifactorial phenomenon that impairs the capacity for dynamic
409 homeostatic adjustments (*63*). Only recently has the scientific community
410 acknowledged altered mechanical properties as a hallmark of ageing (*62*), raising interest
411 for mechanobiological studies in ageing. Our model mimics the structural features of
412 ageing RPE by reducing cell density. This approach isolates the mechanobiological
413 aspects of ageing, allowing for a deeper understanding of how these features develop

414 over time. By using epigenetically 'young' (*64*) cells derived from human induced
415 pluripotent stem cells (hiPSCs), which have undergone rejuvenation-associated
416 reprogramming, we reduced the complexity down to examining how tissue architecture
417 alone impacts mechanical homeostasis and functional capacity, putting aside more
418 complex aspects of biochemical signalling such as oxidative stress. In this system, we
419 were able to recapitulate structural aspects identical to reported remodelling of the aged
420 RPE, such as cell height reduction (*26*), shortening of the apical microvilli (*65*) and
421 presence of actin stress fibers (*27*) by only reducing cell density. This remodelling is
422 possible due to the nearly postmitotic nature of iRPE cells, which cannot use
423 compensatory proliferation as a homeostatic mechanism, but are believed to rely on
424 compensatory cellular hypertrophy (*66*, *67*). We noted that cellular 'hypertrophy' in our
425 model is not merely cell volume enlargement, but 'tissue stretching from within', as we
426 observed cell area enlargement paired with cell height reduction, pointing to individual
427 cell volume conservation. Individual cell area enlargement could also explain the
428 observed microvilli shortening, as microvilli provide membrane reservoirs capable of
429 unfolding to facilitate cell shape changes or to buffer mechanical stress (*68*, *69*).

430 Our work demonstrates for the first time that the age-associated structural phenotype in
431 postmitotic tissue correlates with a shift in the range of mechanical equilibrium. This shift
432 is evidenced by multicellular length-scale stiffening and increased elasticity, with
433 softening at the apical side at the subcellular length scale. Tissue stiffening, in particular
434 increased elasticity, has been reported as a response of epithelial cells to stretch (*68*,
435 *70*), at least in the short term. In our system, the mechanical changes are observed in the
436 long term, four days after the apoptosis-mediated deformation. While stiffening as a
437 characteristic of RPE ageing *in vivo* may be the result of several converging factors,
438 including cell death and ECM remodelling, it is probably mediated by the actin
439 cytoskeleton, as evidenced by another study on epithelial stiffening (*71*) and by our data
440 on extensive transcriptomics changes of actin-related proteins. In particular, the new
441 mechanical equilibrium is accommodated by tissue reinforcement via the formation of
442 transcellular actin stress fibres. This has been reported as a sign of junctional
443 remodelling (*72*) and limiting cell size or elongation during morphogenesis (*73*). Moreover,
444 the strengthening of cell-cell junctions is a known mechanism to support cells in resisting
445 forces (*74*). Interestingly, the non-invasive probing technique of Brillouin microscopy
446 revealed a mismatch between tissue reinforcement and apical cortex remodelling. The
447 observed lower Brillouin shift can be explained by significant changes in the apical cortex
448 composition and in the apical microvilli, which are abundant in actin and tubulin
449 filaments. These filaments enhance the Brillouin shift due to their structural stiffness
450 compared to the underlying cell (*75*). Furthermore, differential remodelling of the apical
451 and lateral cortical actin networks is likely, as is known to happen during morphogenesis
452 (*76*). Notably, the quantified reduction of phosphorylated ezrin indicates decreased
453 cortical tension in AgeD-iRPE, consistent with both our Brillouin measurements and
454 existing literature (*77*). Finally, we were surprised to find that many structural and

455 mechanical adaptations are associated mainly with the apicolateral domains, as a
456 balance between basal cell-ECM adhesion and apical cell-cell adhesion exists and is
457 normally well conserved (*78–80*). This may be attributed to our study conditions, where
458 iRPE cells are cultured on polyacrylamide hydrogels, which provide strictly controlled
459 physical and biochemical cues with a limited possibility for cell-mediated remodelling.
460 Future studies need to elucidate the contribution of ECM cues and cell-mediated ECM
461 remodelling as part of the puzzle of age-related structural remodelling of the outer retina.

462 Our work suggests that age-associated structural phenotype goes hand in hand with
463 actomyosin organisation and remodelling capacity, which affects the RPE function of
464 POS fragments internalisation. Phenotypically, we observe an overall higher contractility
465 and shifts in the expression of nucleators and other actin-related proteins. The apical
466 domain of RPE cells requires high remodelling capacity due to its essentiality for the
467 internalisation function (*43*). In this study, we observed an apicobasal cell remodelling
468 with bulging and lateral relocalisation of cell-cell junctions during the POS internalisation
469 assay, which has not been reported before. The functional significance of these
470 structures remains unclear: do they enhance target grip, increase cortex tension by
471 straightening and thinning the cortical actin mesh, or create a larger apical contact space
472 that allows for unrestricted remodelling of the cortex and membrane, free from reinforced
473 junctions? These observed phenomena may arise from the synergy of conditions in our
474 culture system, where we observe mature cells of nearly three weeks cultured on soft
475 substrates, as opposed to the majority of other studies, which are being conducted on
476 stiff cell culture plastics or glass substrates. In our structurally aged model, we observed
477 a lack of apical bulging and prominent actin-rich protrusions during internalisation. The
478 absence of bulging may stem from the difficulty in disassembling junction-associated
479 structures, which are more reinforced and stable, or from their connection to highly
480 crosslinked or bundled actin structures. A logical explanation is that intercellular
481 reinforcement may redirect actin dynamics to maintain tissue integrity. This could limit
482 the cytoskeletal flexibility required for efficient apical processes, such as phagocytosis,
483 similar to what has been shown in the case of immune cells (*81*). The observed formation
484 of large actin-rich protrusions exclusively in AgeD-iRPE is reminiscent of "arms"
485 structures described in the early embryo (*82*) and may reflect a compensatory
486 mechanism for dispersing phagocytic load. The formation of these protrusions is driven
487 by ARP2/3 activity (*82*), which is highly versatile both in maintaining junctional integrity
488 (*83*), regulating cortical thickness and tension (*57*), as well as playing a major role in the
489 internalisation process (*42*, *46*). Its activity may be diverted towards a new housekeeping
490 maintenance of cortical and junctional actin structure, as opposed to on-demand
491 availability for internalisation. The role of formins in RPE function remains unexplored to
492 date, but our data suggest that they influence phagocytic cup size when inhibited. This
493 effect may occur through alterations in membrane curvature or surface ruffling,
494 impacting the contact area for internalisation. Although supportive of our logic, it is
495 important to underline that the use of SMIFH2 compound might have a secondary effect

496 on myosin II activity (*84*) and be involved in conveying the observed internalisation
497 phenotype. Our findings indicate that structural ageing alters actin network organisation.
498 This change, characterised by prolonged filament stability and a shift in actin usage
499 towards lateral intercellular junctions, limits cytoskeletal responsiveness at the apical
500 surface. Consequently, structural reinforcement takes precedence over dynamic actin
501 remodelling, which is essential for the physiological process of POS phagocytosis.

502 In conclusion, our findings highlight the importance of the form-function paradigm in
503 mechanical homeostasis and ageing tissues. Notably, the relationship between
504 structural reorganisation and ageing is evident in post-mitotic tissues like the retina and
505 brain (*19*, *20*, *85–88*), though it may also apply to proliferative tissues. Further research is
506 necessary to explore how changes in cell density or reorganisation contribute to the
507 functional decay associated with ageing.

508 **METHODS**

509 **Preparation of cell hydrogel substrates**

510 The surface of 20 mm glass-bottom dishes (Cellvis, D35-20-0-N) or 6-well glass bottom
511 plates (Cellvis, P06-1.5H-N) was activated to allow hydrogel attachment by etching with
512 0.1 M NaOH (Merck, 106498), followed by reaction with 4% (3-
513 Aminopropyl)triethoxysilane (Sigma Aldrich, 440140) in isopropanol (VWR, 20842) and
514 final incubation with 1% Glutaraldehyde (Merck, 354400) in double distilled water
515 (ddH2O) (B. Braun, 0082479E).

516 Polyacrylamide hydrogels of 4 kPa stiffness were prepared from an 5%/ 0.1%
517 Acrylamide/Bis-Acrylamide (Bio-Rad 1610140, Bio-Rad 1610142) mixture in ddH2O by
518 radical polymerisation upon addition of the initiators ammonium persulfate (Sigma
519 Aldrich, 248614) at 0.5% (vol/vol) and N'-Tetramethylethylenediamine (Sigma Aldrich,
520 411019) at 0.05% (vol/vol), as previously described (*89*).

521 Hydrogels were trimmed to size of 4 mm before functionalisation with Laminin-511
522 (Biolamina, LN511) and Laminin-332 (Biolamina, LN332) at a concentration of 15 µg/ml
523 respectively. Briefly, a functionalisation solution was prepared from ddH2O, 0.5 M HEPES
524 (Carl Roth, 9105) pH 6, 100% ethanol (Sigma Aldrich, 32205) and 0.2% (vol/vol) Bis-
525 Acrylamide. The solution was degassed for 20 min and was completed by adding 0.2%
526 Di(trimethylopropane)tetraacrylate (Sigma Aldrich, 408360), 3% (wt/vol) Hydroxy-4'-(2-
527 hydroxyethoxy)-2-methylpropiophenone (Sigma, 41089 and 0.03% (wt/vol) Acrylic acid
528 N-hydroxysuccinimide ester (Sigma, A8060) as previously described (*90*). Hydrogels were
529 dehydrated with 70% ethanol for 5 min, incubated under UV for 10 min with the
530 functionalisation solution and washed with 25 mM HEPES and PBS for a total of 20 min
531 before adding the protein solution. The gels were incubated with the protein solution
532 overnight at 4ºC.

533 **Culture of human induced pluripotent stem-cell derived RPE**

534 HiPSCs-derived RPE cells (Fujifilm Cellular Dynamics, R1102) were seeded in 24-
535 wellplates coated with 2.5 µg/ml vitronectin XF (StemCell Technologies, 07180). Cells
536 were cultured in MEM-alpha with nucleosides (Thermo Fisher, 12571063), supplemented
537 with 1x Glutamax (Thermo Fisher, 35050061), 5% (vol/vol) Knockout Serum replacement
538 (Gibco, 10828028), 1% (vol/vol) N2-Supplement (Gibco, 17502048), 55 nM
539 Hydrocortisone (Sigma Aldrich, H6009), 250 µg/ml Taurine (Sigma Aldrich, T8691),
540 14 pg/ml Triiodo-L-thyronine (Sigma Aldrich, T5516) and 25 µg/ml gentamycin (Gibco,
541 15750060) following the manufacturer's instructions. The medium was exchanged every
542 other day. For seeding on hydrogels, cells were detached from the 24-wellplate by 30 min
543 incubation with 5 mM PBS/EDTA (Sigma Aldrich, E6511), followed by 5 min incubation
544 with TrypLE Express (Gibco,126050). Cells were seeded on the UV-sterilized
545 functionalised hydrogels at 5000-6000 cells/mm^2. The medium of cells on hydrogels was
546 exchanged halfway twice a week.

547 **On-demand apoptosis for Apoptosis-generated Density (AgeD)**

548 Apoptosis was induced by expression and on-demand dimerisation of recombinant
549 FKBP-caspase8 (FKBP-casp8) fusion protein (*35*). The FKBP-casp8 containing plasmid
550 was delivered packaged in AAV5 (VectorBuilder, VB230127-1043eaq). Briefly, on day 10
551 after seeding on the hydrogel, cells were transduced with the virus at 7x10^6 infectious
552 units per cell for 24 h. On day 15, 120 h after the transduction, FKBP-casp8 was dimerised
553 by addition of 100 nM AP20187 in medium (Sigma Aldrich, SML2838) for 24 h. Paired
554 control monolayers were also subjected to the AP20187 treatment. The read-out was
555 performed on day 20, or 96 h after apoptosis treatment finalisation.

556 **Virus, mixed and medium-transfer controls**

557 To exclude effects of the AAV as a delivery system, we used an AAV5-packaged construct
558 that promotes the expression of green fluorescent protein (GFP) (VectorBuilder,
559 VB10000-9287ffw) as a control. Cells were transduced and treated the same way as
560 described for FKBP-casp8 expressing cells, including same timing of viral transduction,
561 AP20187 treatment and read-out.

562 To obtain a mixed population of transfected and naïve cells, two days prior to seeding on
563 hydrogels, we transduced hiPSCs-derived RPE in a 24-well plate at 7x10^6 infectious units
564 per cell for 24 h with the FKBP-casp8 vector (VectorBuilder, VB230127-1043eaq). The
565 virus solution was replaced with fresh medium after 24 h. After another 24 h, we seeded
566 a 10%/90% mixture of the transduced hiPSCs-derived RPE cells and naïve hiPSCs-
567 derived RPE on the hydrogels as described above. On day 15, corresponding to the same
568 apoptosis timing of AgeD treatment, apoptosis was induced by addition of 100 nM
569 AP20187 (Sigma Aldrich, SML2838) for 24 h. The read-out was performed at 96 h after
570 apoptosis treatment finalisation.

571 To exclude possible effects of the release of apoptotic debris during the apoptosis, 16 h
572 after AP20187 addition, the medium from AgeD samples was transferred onto control
573 conditions. The medium was then replaced after apoptosis treatment finalisation. 24 h
574 after apoptosis finalisation, the medium from AgeD samples was again transferred to
575 control samples and the samples were maintained in this conditioned medium until read-
576 out.

577 **EdU incorporation-based proliferation assay**

578 Proliferation was assessed by evaluating the incorporation of the base 5-Ethinyl-2'-
579 Desoxyuridin (EdU) with the Click-iT EdU kit (Thermo Fisher, C10337). Cells were
580 incubated with 1:1 mixture of 20 µg/ml EdU and cell culture supernatant for 24 h. The
581 subsequent EdU development reaction was performed following the manufacturer's
582 instructions. Monolayers were imaged completely as overviews of stitched tiles at
583 inverted epi-fluorescent microscope Zeiss Axio Observer 7. Positive cells were identified
584 by using the particle analysis tool in Fiji and their number was normalised to the total
585 number of cells, as detected by DNA labelling by DAPI (1 µg/ml, Invitrogen D1306).

586 **Photoreceptor fragment phagocytosis assay**

587 Photoreceptor outer segment fragments were isolated from porcine eyes obtained from
588 a local slaughterhouse and labelled with FITC (Thermo Fisher, F1906) as previously
589 described (*91*). For the assay, the vial was thawed and washed with medium at 2300 g for
590 5 min. The pellet was resuspended in complete hiPSCs-derived RPE medium together
591 with the bridging molecules human Protein-S (Coachrom, pp012A) at 2 µg/ml and human
592 MGF-8 (R&D Systems, 2767-MF-050) at 2.4 µg/ml. An approximate ratio of ten
593 photoreceptor outer segment fragments per RPE cell seeded was used. Cells were
594 incubated for 4 h, washed four times with DPBS with Ca^{2+} and Mg^{2+} (Gibco, 14040117) and
595 fixed with 2% paraformaldehyde (Merck, 818715) for 8 min at room temperature (RT).
596 Samples were then permeabilised with 0.3% Triton-X-100 (Sigma Aldrich, T8787) for 2 min
597 and labelled for actin with Phalloidin AF568 (Molecular probes, A12380). Three z-stacks
598 per monolayer were recorded at Zeiss LSM710 Confocal Microscope with ZEN Black
599 software with 40x water immersion objective (ZEISS, 420862-9970-000) in Airyscan super
600 resolution mode. The subsequent analysis was performed in Imaris v10.2.0 (Oxford
601 Instruments).

602 **Nanoindentation and dynamic mechanical analysis**

603 Nanoindentation was performed on a Chiaro Nanoindentor (Optics 11 Life) mounted on
604 an inverted epifluorescence microscope Zeiss Axio Observer 7 with environmental
605 control. Measurements were performed on living cells in displacement control mode
606 using a spherical probe of 20 µm diameter and 0.025 N/m stiffness. Three matrix scans
607 of 16 indentations were recorded per monolayer, indenting 6 µm into the cells. Dynamic
608 mechanical measurements were performed at 1, 2, 4 and 10 Hz to allow for viscoelastic

609 characterisation. For the analysis, indentation portions between the contact point and
610 2.5 µm were fitted using the Hertz model in the Optics 11 Analysis Software, allowing a
611 range for the contact point fit of 30% of the maximum load. Effective Young's modulus
612 values of fit R^2 better than 0.95 were used for further statistics. Loss and storage moduli
613 were determined for the different frequencies (1 Hz, 2 Hz, 4 Hz and 10 Hz) using the
614 software default methods.

615 **Immunofluorescent labelling and imaging**

616 Monolayers on hydrogels were fixed with 2% paraformaldehyde (Merck, 818715) for 8 min
617 at RT and permeabilised with 0.3% Triton-X-100 (Sigma Aldrich, T8787) for 2 min at RT.
618 Samples were then blocked with 1% BSA (Serva, 11930) in PBS for 30 min at RT, followed
619 by incubation with primary antibodies (Table 1) in blocking solution overnight at 4ºC. After
620 washing, secondary antibodies (Table 1) diluted in PBS were added for 2 h at RT. Samples
621 were washed and mounted in Mowiol mounting medium (Carl Roth, 9002-89-5) before
622 imaging. Unless started otherwise, samples were imaged at Zeiss LSM710 Confocal
623 Microscope with 40x water immersion objective (ZEISS, 420862-9970-000) in Airyscan
624 super resolution mode as z-stacks of 0.5 µm optical slicing. Uniform imaging settings
625 were used between samples within the same experiment. Images were then inspected
626 and further processed for different analyses using Fiji (*92*).

627 **Bulk RNA sequencing**

628 RNA isolation for RNA sequencing was performed using the RNeasy Micro RNA isolation
629 kit (Qiagen, 74004) with DNase treatment following the manufacturers protocol. Bulk
630 RNA sequencing was performed by the Life & Brain NGS Core Facility (Bonn, Germany)
631 after QuantSeq 3'-mRNA Library Prep/ Lexogen enrichment at NovaSeq 6000 with a depth
632 of 20M reads. The raw data was processed using nf-core/rnaseq v3.12.0
633 (https://doi.org/10.5281/zenodo.1400710) of the nf-core collection of workflows (*93*).
634 The pipeline was executed with Nextflow v23.04.1 (*94*). The complete data set is available
635 on the Gene Expression Omnibus repository (GEO accession number GSE297557).
636 Differential expression analysis was performed using DESeq2 package (*95*) in R, applying
637 an alpha of 0.05. Genes were considered differentially expressed at an adjusted p-value
638 lower than 0.1. Heatmaps were generated from the DESeq data set after z-normalisation
639 using the package pheatmap (*96*) and a custom-curated gene list. Functional enrichment
640 of terms related to differentially expressed genes was performed using the g:Profiler
641 online tool (*97*) using the terms GO molecular function, GO cellular component and GO
642 biological process as well as the pathways KEGG, Reactome and WikiPathways. For
643 comparison, publicly available data on the ageing human RPE was obtained from Butler
644 et al.(*49*) and Cai et al. (*48*).

645 **Immunoblotting**

646 Samples were harvested using RIPA buffer (*98*) with phosphatase inhibitors PhosSTOP™
647 (Roche, 4906845001) and were subjected to DNA digestion for 15 min by Pierce Universal
648 Nuclease for cell lysis (Thermo Fischer, 88700) prior to addition of Lämmli buffer (*99*).
649 Samples were then heated to 95 ºC for 7 min and ca. 10 µg were loaded onto a 10 to 14%
650 (depending on target protein molecular weight) polyacrylamide gel (*100*) for SDS-PAGE
651 together with a ProSieve Quadcolor Protein Marker (Lonza, 00193837). Proteins were
652 blotted onto Immobilion-P PFDV membrane (Thermo Fischer 88518) and labelled with
653 primary and secondary antibodies for different targets (Table 1). Bands were detected at
654 the Fusion Solo (Vilber Lourmat) after detection with the Pierce™ ECL Western blotting
655 substrate (Thermo Fischer, 32106). The signal was quantified in Fiji (*92*) by using equal-
656 sized region of interest (ROI) for all bands and measuring the mean grey value. The
657 measurements for the proteins of interest were normalised to the housekeeping protein
658 GAPDH.

659 **Modulation of actin nucleator activity**

660 Actin nucleation by ARP2/3 was modulated by using CK-666 (Tocris Bioscience, #3950)
661 at 500 nM in medium. After 1 h incubation, the monolayers were characterised by
662 nanoindentation. For phagocytosis studies, the monolayers were incubated for 30 min
663 with 500 nM CK-666, followed by incubation with the photoreceptor fragments and the
664 bridging molecules in CK-666 containing medium for 4 h. For modulating formin activity,
665 20 µM SMIFH2 (Tocris Bioscience, #4401) was used instead keeping the same timing and
666 procedure. DMSO at a paired concentration was used as carrier control.

667 **Analysis of extrusion events**

668 Extrusion events were quantified from live cell imaging of apoptosis induction on SiR-
669 Actin (Spirochrome, SC001) labelled cells. The last 15 hours of apoptosis induction were
670 used for the quantification which relies on extrusion events being visible as very bright
671 spots. The video was aligned to correct for stage shifts, smoothed using a Gaussian filter
672 and overlayed in a maximum intensity z-projection in Fiji. The resulting image was
673 thresholded to generate a binary mask and extruded cells were counted using the particle
674 analysis tool in Fiji.

675 **Analysis of cell density**

676 Cell density was quantified from snaps of nuclear staining obtained on epi-fluorescence
677 microscope at 20x magnification. Three to four snaps were used per condition per
678 experiment. Nuclear signal was smoothed using a Gaussian filter, then detected by
679 thresholding. The binary mask was subjected to watersheding and the number of nuclei
680 was counted by using the particle analysis tool in Fiji. Density was calculated by dividing
681 the obtained nuclei count to the area of the field of view. Data originates from at least
682 three independent experiments.

683 **Analysis of cell height**

684 Cell height was determined from super resolution z-stacks of F-actin staining in cross-
685 sectional view. Cells were imaged fixed after mounting in Mowiol, which leads to lower
686 absolute height compared to the height detectable in live-cell imaging. Ten cells per stack
687 were measured with the line tool in three stacks per condition from three independent
688 experiments.

689 **Analysis of cell outline segmentation and shape factor calculation**

690 Cellular outlines from F-actin labelling were segmented using cellpose (*101*). The
691 generated regions of interest (ROI) were imported in Fiji and the cell area and perimeter
692 were measured to calculate the dimensionless shape factor (*102*, *103*).

693 **Analysis of stress fibres**

694 Cells with stress fibres were manually counted using the multipoint tool in Fiji and
695 normalised to the cell number as calculated after segmentation of cells via cellpose.

696 **Analysis of microvilli length**

697 Microvilli length was characterised from cross-sectional views of ezrin labelling in Fiji.
698 Briefly, at least three cross-sections from at least three stacks per condition from three
699 independent experiments were blurred with a Gaussian blur and a threshold was applied
700 to capture the structure. The resulting masks were selected via the magic wand tool and
701 an eclipse fit was performed. The minor axis was used as an approximate measure of the
702 microvilli length.

703 **Photoreceptor fragment phagocytosis analysis**

704 The photoreceptor fragment phagocytosis was characterised using the Software Imaris
705 v10.2.0 (Oxford Instruments). Briefly, the actin labelling was used to create a surface
706 capturing only the apical actin portion of the monolayer. The average z-position of the
707 surface was determined as a cuff-off height to distinguish internal vs external particles.
708 Separately, photoreceptor fragments were segmented as a surface and the cut-off height
709 was used to distinguish between internalised and external fragments. The count and
710 volume of the fragments of both populations was recorded and used for further analysis.

711 **Quantification of apical actin area**

712 The apical actin area of 300 x 300 pixel field of view was segmented from z-stacks of
713 phalloidin staining during photoreceptor internalisation as a surface in Imaris v10.2.0
714 (Oxford Instruments). For the region of interest, only a set number of slices including the
715 same upper portion of the cell monolayer were used. The covering area, as internally
716 determined by the software, was then noted.

717 **Quantification of vinculin junctional to cytoplasmic ratio**

718 Junctional signal of vinculin was quantified as a ratio of junctional to cytoplasmic mean
719 grey value in single optical sections. For this, paired F-actin signal was used to segment
720 cell outlines via cellpose as described above. The generated ROIs were imported in Fiji
721 and a custom macro was used to 'slim-down' the ROIs, invert the mask, watershed the
722 signal and generate ROIs that encompass the junctional regions around cells. The
723 generated junctional ROIs were used to measure grey value as an average per image. The
724 'slimmed-down' cell ROIs were used to measure the cytoplasmic signal. The average
725 values of junctional and cytoplasmic signals per image were used to generate the
726 junctional to cytoplasmic vinculin measurements.

727 **Quantification of junctional pMLC2**

728 Paired samples from the same experiment were stained with the same antibody solution
729 and imaged with the same imaging settings. In single optical sections at the junctional
730 level, pMLC2 signal was thresholded in Fiji making sure the junctional signal is captured.
731 The mean grey value was measured only within the thresholded region. At least three
732 images were measured per condition per experiment.

733 **Quantification of MRTFA**

734 MRTFA was quantified as nuclear to cytoplasmic ratio of the mean grey value. For this,
735 paired cell nuclei signal (DAPI staining) was segmented via cellpose to generate nuclear
736 ROIs. Nuclear MRTFA was measured as average of the mean grey value of all nuclei ROIs
737 within the image. Cytoplasmic MRTFA was measured after setting nuclear ROIs pixels as
738 zero and thresholding the rest of the image. Then, the mean grey value of the thresholded,
739 non-zero region was measured.

740 **Brillouin microscopy**

741 Brillouin imaging was performed using a commercial setup based on an inverted Nikon
742 Ti-2 Eclipse microscope using a vertically polarised, continuous-wave laser (Cobolt
743 Flamenco, λ = 660 nm, ~ 100 mW) beam with a temperature-tuned air-spaced etalon
744 (LightMachinery) attenuated by 0.6 optical density (OD) filter, resulting in approximately
745 9 mW incident power at the sample. Light was coupled into a confocal circulator
746 (LightMachinery, HF-13311) and directed to the microscope through a polarising beam
747 splitter and a quarter wave plate (QWP) yielding circularly polarised light. Measurements
748 were performed on a motorised translation stage (Prior Scientific, H117E2NN) using an
749 air objective (Nikon S Plan Fluor 20X NA 0.45), achieving an estimated 0.73 µm lateral and
750 6.52 µm axial resolution. Brightfield and fluorescence imaging were performed
751 sequentially using a Teledyne sCMOS camera and epi-fluorescence illumination (Nikon
752 D-LEDi).

Backscattered Rayleigh and Brillouin signals were collected with the same objective and routed back through the confocal circulator. The Brillouin signal was acquired using a LightMachinery HyperFine spectrometer (HF-8999-PK-660), equipped with a “pump killer” (PK) module with an air-spaced, pressure-tuned etalon to suppress the elastically scattered Rayleigh light and laser line reflection (~ 60 dB attenuation). Frequency-shifted Brillouin Stokes and anti-Stokes components were directed into the spectrometer, comprised of a virtually imaged phase array (VIPA) and a reflective echelle diffraction grating for spectral dispersion. The cross-dispersed orders were focused onto the CMOS camera sensor (Hamamatsu ORCA-Fusion, C14440-20UP) simultaneously acquiring the full spectrum. The typical acquisition time of a single spectrum is 500 ms, with a spectral resolution < 1 pm.

Spectral data acquisition and raster scanning was facilitated with LightMachinery LabView-based software. The x-y pixel coordinates on the CMOS sensor are converted to wavelength (or frequency) and a Lorentzian fit is applied over each Brillouin peak as described by equation (1).

$$I(\omega) = \frac{I_0}{\pi} \frac{\Gamma \omega_B^2}{(\omega^2 - \omega_B^2)^2 + \Gamma^2 \omega_B^2} \tag{1}$$

The final Brillouin shift ω_B and linewidth Γ values for a given spectrum were computed by averaging the corresponding values from the Stokes and anti-Stokes peaks forming a single voxel in the raster scan. Z-scans were acquired as a 3x3 matrix in a step size of 20 µm and z-step of 2 µm, z-range of 80 µm, while apical and basal scans were acquired over the region of 50 x 50 µm with a lateral step size of 1.5 µm. The z-position of apical and basal Brillouin scans within the monolayer was selected based on the appearance of the cells in brightfield and SiR-actin fluorescence images. The scans were limited to 15 minutes to obtain an optimal raster scan resolution while maintaining the cell viability. It should be noted that although the average laser power at sample is within the range used in biological samples, by comparing brightfield images taken before and after the Brillouin scan, some deformation of the sample was observed. This could have occurred due to the heat of the laser affecting the gel or the cells as the RPE cells’ pigmentation contributes to the linear laser light absorption.

Brillouin shift data analysis

For segmentation, the Brillouin shift maps from basal layers were linearly scaled and converted into 8-bit grayscale images, proportionally reflecting the original Brillouin shift values. The grayscale images were segmented using cellpose to identify the individual structures within the images. Following segmentation, two populations were defined: "core", corresponding to segmented regions, and "interstitium", corresponding to areas between them. These modified images were then imported into a custom-written MATLAB script, where appropriate binary masks were created and applied to the original

Brillouin shift maps to separate the “core” and the “interstitium”. For each raster scan, the mean Brillouin shift and the standard deviation was calculated separately for the two regions. The 3 x 3 raster z-scans resulted in 9 representative z-axis line profiles per region, capturing mechanical transition across the sample. Each profile typically displayed a stiffness change from the hydrogel to the monolayer and then from the monolayer to the surrounding cell media. For each sample, 5 of these scans were obtained.

The Brillouin Shift data was imported into a custom-written MATLAB script to identify the local peaks or, where absent, plateaus in the Brillouin shift profiles (https://github.com/GiedreAstra/Example_E3_zscan_RPE.git). Each line profile was smoothed with a Savitzky-Golay filter, the peak was detected using MATLAB’s findpeaks function, with a minimum width imposed to prevent false peak identification. A gradient of the filtered z-line was taken. To refine peak localisation, a Gaussian fit was applied across a range of filtered Brillouin shift values. The fitting range was bound by the z-positions at which the local maximum and the minimum of the derivative of the z-line was within an appropriate range from the previously identified peak. The fitted peak value and position were retrieved. In the case of no peak detection, the code identifies the onset of a drop in the plateau by considering the change in the derivative over a moving average window. The corresponding plateau value was then recorded. The performance of the script was checked for individual z-profiles to exclude outliers.

DECLARATION OF AI USE

The preparation of this manuscript has been aided by AI-assisted technologies to improve its readability and language.

ACKNOWLEDGMENT

We would like to acknowledge all the members of the REMeD group in the past years for their contributions to the discussion of the work. Moreover, we appreciated Adam Breitscheidel's technical support in graphic design and Gloria’s excellent help in imaging. We would like to acknowledge the support of Chris Davis from the Centre for Virus Research of the University of Glasgow for providing a lab space in Garscube campus to enable AAV work needed for the sample preparation for Brillouin microscopy.

FUNDINGS

This work in Di Russo’s laboratory was supported by: A grant from the Interdisciplinary Centre for Clinical Research within the Faculty of Medicine at the RWTH Aachen University and German Research Foundation (DFG; RU 2366/3-1). Furthermore, J.D.R. and W.W. are supported by the DFG within 363055819/GRK2415.

The collaboration with Vassalli’s lab for Brillouin microscopy was supported by: RS MacDonald Facility Access funding grant by the Scottish Universities Life Sciences

Alliance (SULSA). A travel grant by the German Academic Exchange Service (DAAD) program number 57745342 and a travel grant by Boehringer Ingelheim Fonds.

A.N.K. and T.P. are supported by Add-on Fellowships of the Joachim Herz Foundation.

AUTHORS CONTRIBUTION

JDR conceived and supervised the project. TP designed and performed all the experiments. ANK supported the establishment of the iRPE culture on PAA gels. GA, ANK and TP performed Brillouin measurements. GA and ANK performed Brillouin analysis. MM performed initial transcriptomics data analysis and advised on the transcriptomic exploration. RR supported the immunoblotting experiments. SS supported with confocal imaging. LY supported the establishment of viral transduction. WW and MV supported the work with expertise and advice. JDR and TP wrote the manuscript, and all authors discussed and commented on it.

COMPETING INTERESTS

Authors declare that they have no competing interests.

Data and materials availability

All data are available in the main text or the supplementary materials. Furthermore, the complete data set of RNA bulk sequencing is available on the Gene Expression Omnibus repository (GEO accession number GSE297557).

Supplementary figures

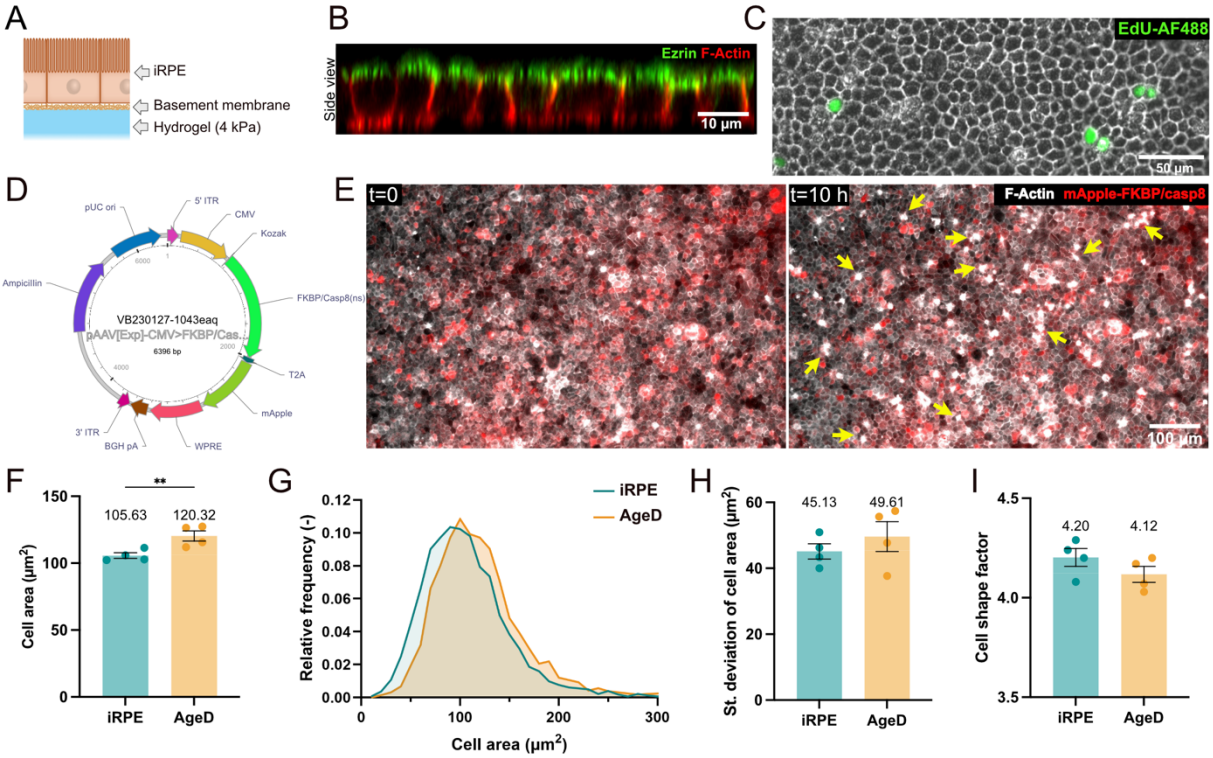

Suppl. figure 1: The iRPE and AgeD-iRPE model and cell morphometric characterisation. A: Schematics of iRPE cell culture system displaying the monolayer obtained on 4 kPa hydrogels functionalised with basement membrane mimicking coating. **B:** Cross-section of iRPE after 20 days of culture labelled for F-actin (red) and ezrin (green) showing characteristic apicobasal polarisation. **C:** Representative micrograph of proliferation assay showing iRPE cells in brightfield and proliferating cell nuclei labelled by EdU-AF488 (green). **D:** Map of plasmid used for the expression of pro-apoptotic FKBP-casp8 protein and delivered to iRPE cells by AAV5. **E:** Representative micrographs of SiR-actin labelled iRPE (white) expressing mApple as fluorescent reporter (red) at the timepoint of AP20187 addition and 10 h afterwards. Extrusion events of apoptotic cells at the latter point are indicated with yellow arrows. **F:** Quantification of average cell area. **G:** Relative frequency distribution of cell areas. **H:** Standard deviation of cell areas within an experiment. **I:** Average cell shape factor. Datapoints represent average values ± SEM per experiment originating from 4 independent experiments. Statistical significance was tested using a paired t-test, where **: $p<0.01$.

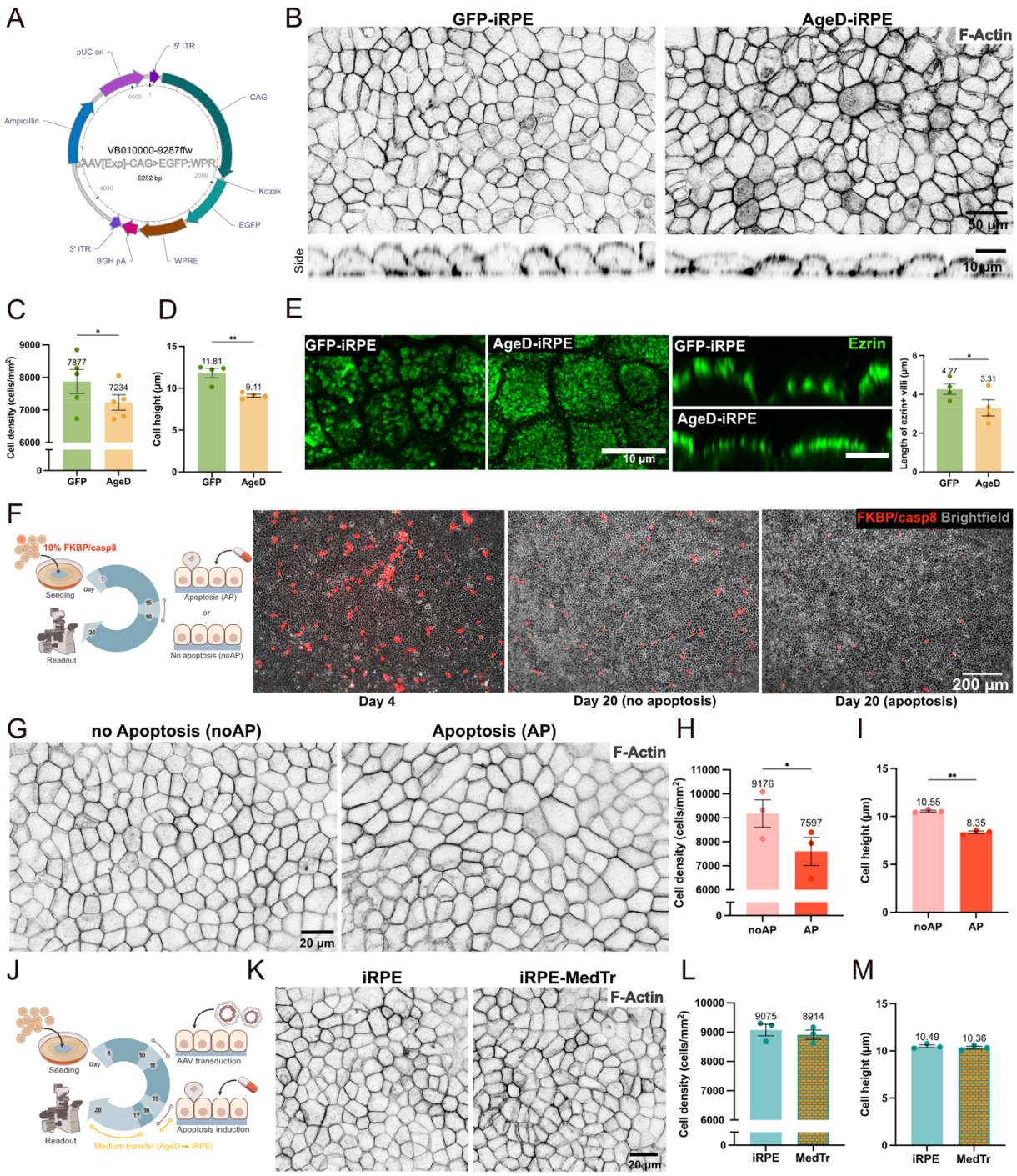

Suppl. figure 2: Controls for influence of virus, recombinant FKBP-casp8 protein expression and debris released into medium. A: Vector map of plasmid used as viral control, which promotes the expression of GFP. **B:** Representative micrographs of F-actin in GFP-iRPE compared to AgeD-iRPE (top) and cross sections (down). **C:** Quantification of average cell density for GFP-iRPE. **D:** Quantification of cell height for GFP-iRPE. **E:** Representative micrographs showing ezrin as maximum intensity projection in top (left) and side views (middle) and the quantification of ezrin-positive microvilli length (right). **F:** Experimental schematics of mixed population control. The micrographs show representative monolayers of mApple-positive transduced cells within the naïve cells at day 4 and at day 20 (the readout day). **G:** Representative micrographs of F-actin labelled mixed population iRPE without apoptosis induction (noAP) and after induction of apoptosis (AP). **H:** Quantification of average cell density for the mixed population control. **I:** Quantification of cell height for the mixed population control. **J:** Experimental schematics of medium-transfer control **K:** Representative micrographs of F-actin labelled control monolayers vs. monolayers subjected to medium transfer. **L:** Quantification of average cell density for the medium transfer control. **M:** Quantification of cell height for the medium transfer control. Datapoints represent average values per experiment ± SEM originating from 3 to 5 independent experiments. Statistical significance was tested using a paired t-test, where *: $p<0.05$, **: $p<0.01$.

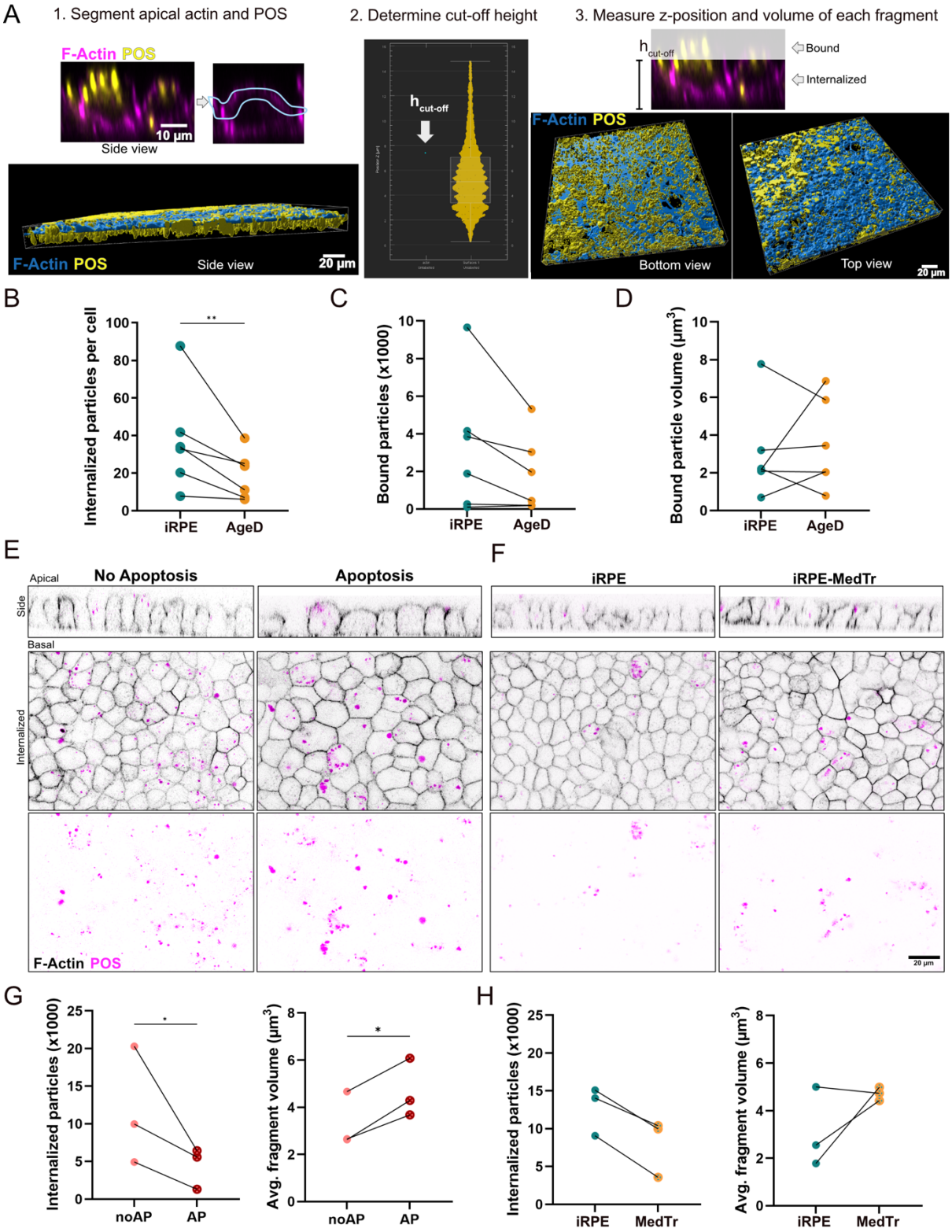

Suppl. figure 3: POS internalisation assay. A: Workflow for 3D segmentation, cut-off height determination and classification into 'bound' vs 'internalised' particles. **B:** Quantification of number of internalised POS particles normalised to cell number. **C:** Quantification of bound POS particles number in the field of view. **D**: Quantification of average bound POS particle volume. **E:** Representative micrographs of iRPE at t = 4 h of POS internalisation assay as orthogonal cross-sections (up) or as single optical slices in the middle of cells (lower two panels) for the "mixed" control. **F:** Representative micrographs of iRPE at t = 4 h of POS internalisation assay as orthogonal cross-sections (up) or as single optical slices in the middle of cells (lower two panels) for the medium-transfer control (MedTr). **G:**

884 Quantification of POS fragments internalised within the time of the assay per field of view (left) and quantification of
885 the average volume of internalised fragments (right) for the "mixed" population control. **H:** Quantification of POS
886 fragments internalised within the time of the assay per field of view (left) and quantification of the average volume of
887 internalised fragments (right) for the medium-transfer control. Datapoints represent average values per experiment
888 originating from 3 to 6 independent experiments. Statistical significance was tested using a paired t-test, where *:
889 p<0.05, **: p<0.01.

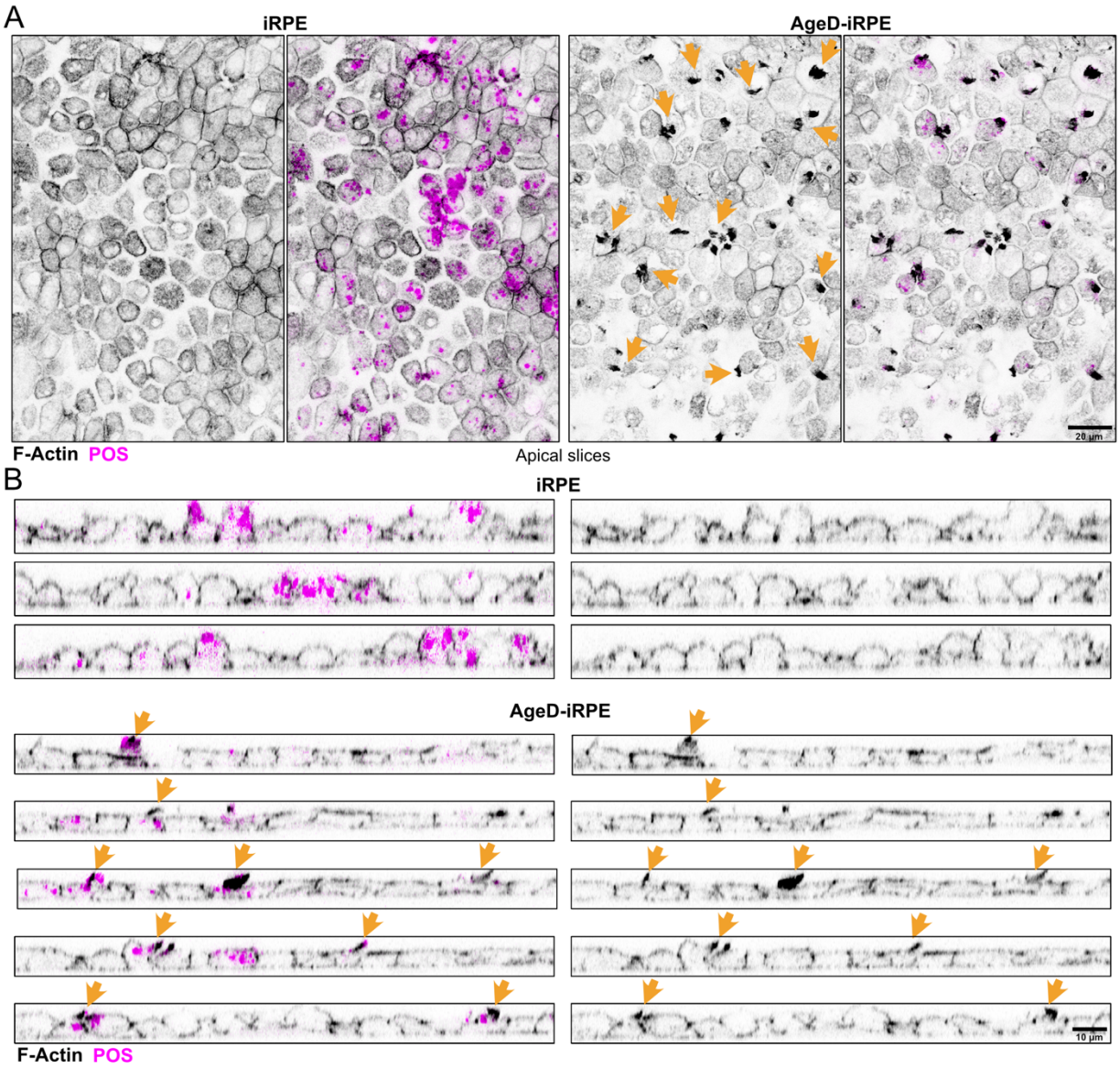

890

891 **Suppl. figure 4: Differential apical actomyosin remodelling between iRPE and AgeD-iRPE during POS**
892 **internalisation assay. A:** Representative micrographs of the apical side of monolayers during internalisation showing
893 F-actin and photoreceptors. Arrows point to the presence of protruding actin-rich structures in AgeD-iRPE. **B:**
894 Representative orthogonal cross sections of iRPE and AgeD-iRPE monolayers during internalisation showing F-actin
895 and FITC-labelled POS. Arrows point to actin-rich structures.

A

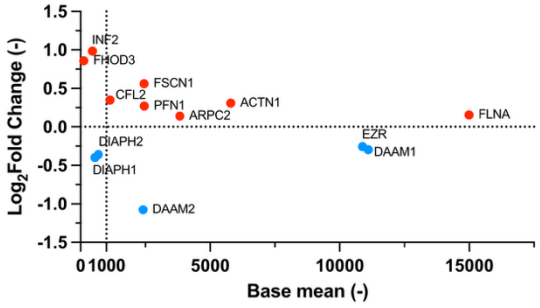

B

Overlapping DEGs with reported age-related changes in humans

Gene symbol	Protein name	Direction change
Cai H. et al. 2012 (DOI:10.3389/fnagi.2012.00008)		
DKK1	dickkopf WNT signaling pathway inhibitor 1(DKK1)	up
LAMA3	laminin subunit alpha 3(LAMA3)	up
TYMS	thymidylate synthetase(TYMS)	up
PLEKHG4	pleckstrin homology and RhoGEF domain containing G4(PLEKHG4)	down
SCN2B	sodium voltage-gated channel beta subunit 2(SCN2B)	down
Butler J. M. et al. 2021 (DOI: 10.1111/jcmm.16569)		
AKAP6	A-kinase anchoring protein 6(AKAP6)	up
BMP8B	bone morphogenetic protein 8b(BMP8B)	up
CCDC51	coiled-coil domain containing 51(CCDC51)	up
CTSV	cathepsin V(CTSV)	up
DUSP6	dual specificity phosphatase 6(DUSP6)	up
KL	klotho(KL)	up
SLC6A20	solute carrier family 6 member 20(SLC6A20)	up
TNFRSF10C	TNF receptor superfamily member 10c(TNFRSF10C)	up
TRPV4	transient receptor potential cation channel subfamily V member 4(TRPV4)	up
CPAMD8	C3 and PZP like alpha-2-macroglobulin domain containing 8(CPAMD8)	down
CSRP2	cysteine and glycine rich protein 2(CSRP2)	down
DCT	dopachrome tautomerase(DCT)	down
GAS1	growth arrest specific 1(GAS1)	down
TMEM150C	transmembrane protein 150C (TMEM150C)	down

C

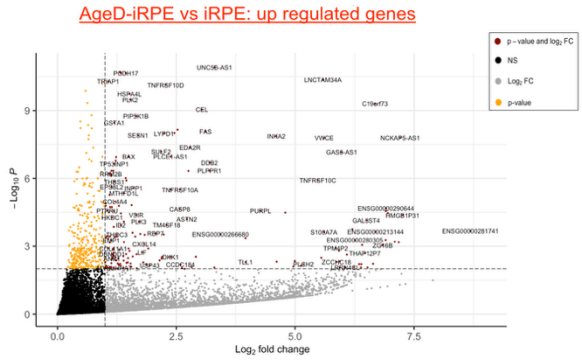

D

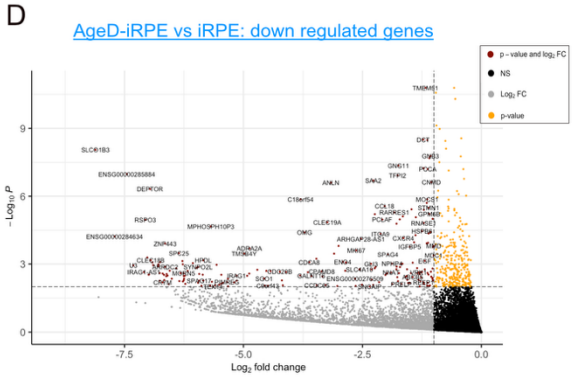

Suppl. figure 5: AgeD-iRPE shows a differential gene expression from iRPE, which is partly overlapping with ageing patients. A: Base mean vs Log2Fold change for significantly differentially expressed actin-associated genes in AgeD-iRPE vs iRPE. **B:** Differentially expressed genes (DEGs) overlapping with the results from studies on ageing human RPE from Cai H. et al. *(48)* and Butler J. M. et al. *(49)* . Gene names are labelled in blue or red for downregulated or upregulated, respectively. **C:** Volcano plot of upregulated DEGs between AgeD-iRPE and iRPE. **D:** Volcano plot of downregulated DEGs between AgeD-iRPE and iRPE. Cut-off lines were drawn at log2fold=1, corresponding to a fold change of two, and at log10P = -2, corresponding to a p of 0.001 and padj of 0.1, which we set as cut-off significance value for DEGs. Genes are assigned to groups based on their log2fold and log10fold values as highlighted in the legend.

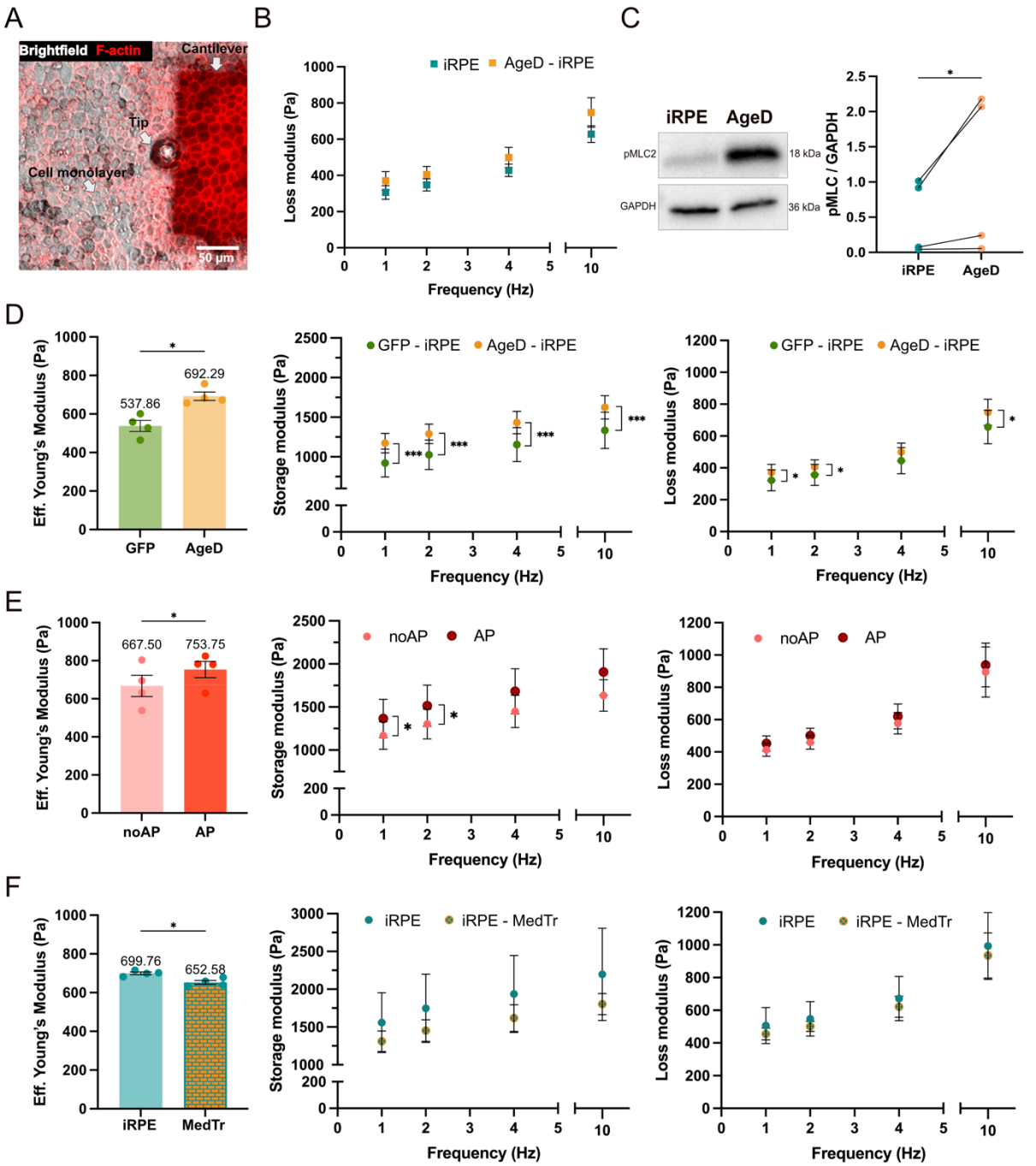

Suppl. figure 6: Biomechanical characterisation of iRPE conditions. A: Experimental setup for performing nanoindentation. The micrograph shows a top view of SiR-actin labelled cell monolayer and cantilever with tip. **B:** Average loss modulus of iRPE and Aged-iRPE. **C:** Immunoblot of pMLC2 and GAPDH as a housekeeping protein and quantification of total pMLC2 protein from immunoblots, normalised to GAPDH. **D:** Average Effective Young's modulus, storage and loss moduli for virus control. **E:** Average Effective Young's modulus, storage and loss moduli for treated (noAP) and untreated (AP) mixed population iRPE. **F:** Average Effective Young's modulus, storage and loss moduli for iRPE and conditioned medium treated iRPE (MedTr-iRPE). Datapoints represent average values ± SEM per experiment originating from 3 to 4 independent experiments. Statistical significance was tested using a paired t-test, where *: $p<0.05$ and ***: $p<0.001$.

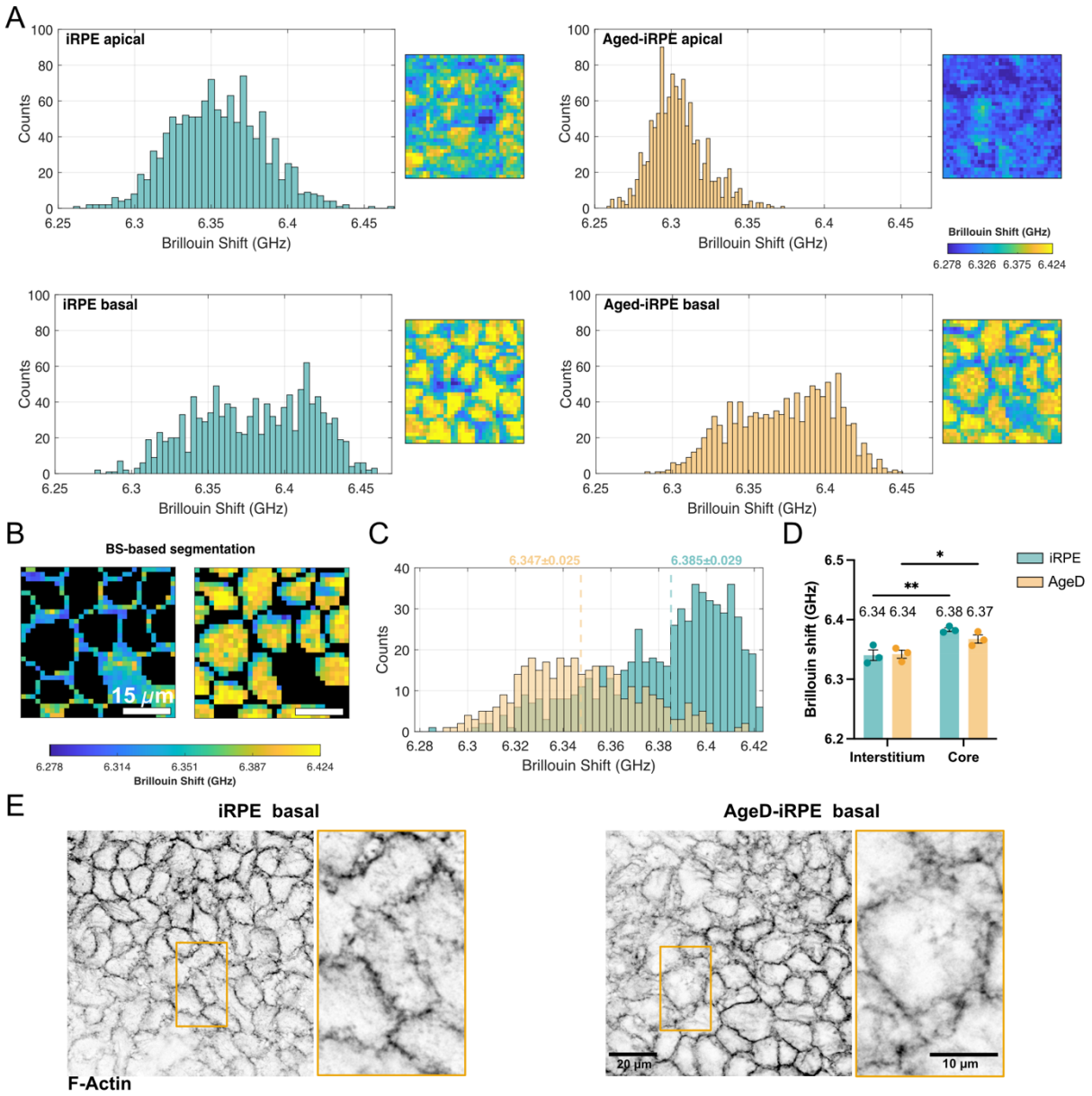

Suppl. figure 7: Distribution of Brillouin shift values in apical and basal layers of iRPE and AgeD-iRPE and segmentation of Brillouin shift values from basal maps. A: Representative histograms of iRPE and AgeD-iRPE basal and apical Brillouin shift values acquired from 50 x 50 µm regions of interest and the respective plots. **B:** Representative plots of segmented Brillouin shift maps with two population modes defined by Cellpose segmentation (see Methods). **C:** Representative histogram of the plots shown in B illustrating the identified populations. **D:** Quantification of Brillouin shift population modes named as "Interstitium" and "Core" in basal iRPE and AgeD-iRPE monolayers. **E:** Representative F-Actin micrographs of basal iRPE and AgeD-iRPE monolayers with annotated regions enlarged. Datapoints represent average values per experiment ± SEM originating from 3 independent experiments. Statistical significance was tested using a ratio paired t test, where *: $p<0.05$ and **: $p<0.01$.

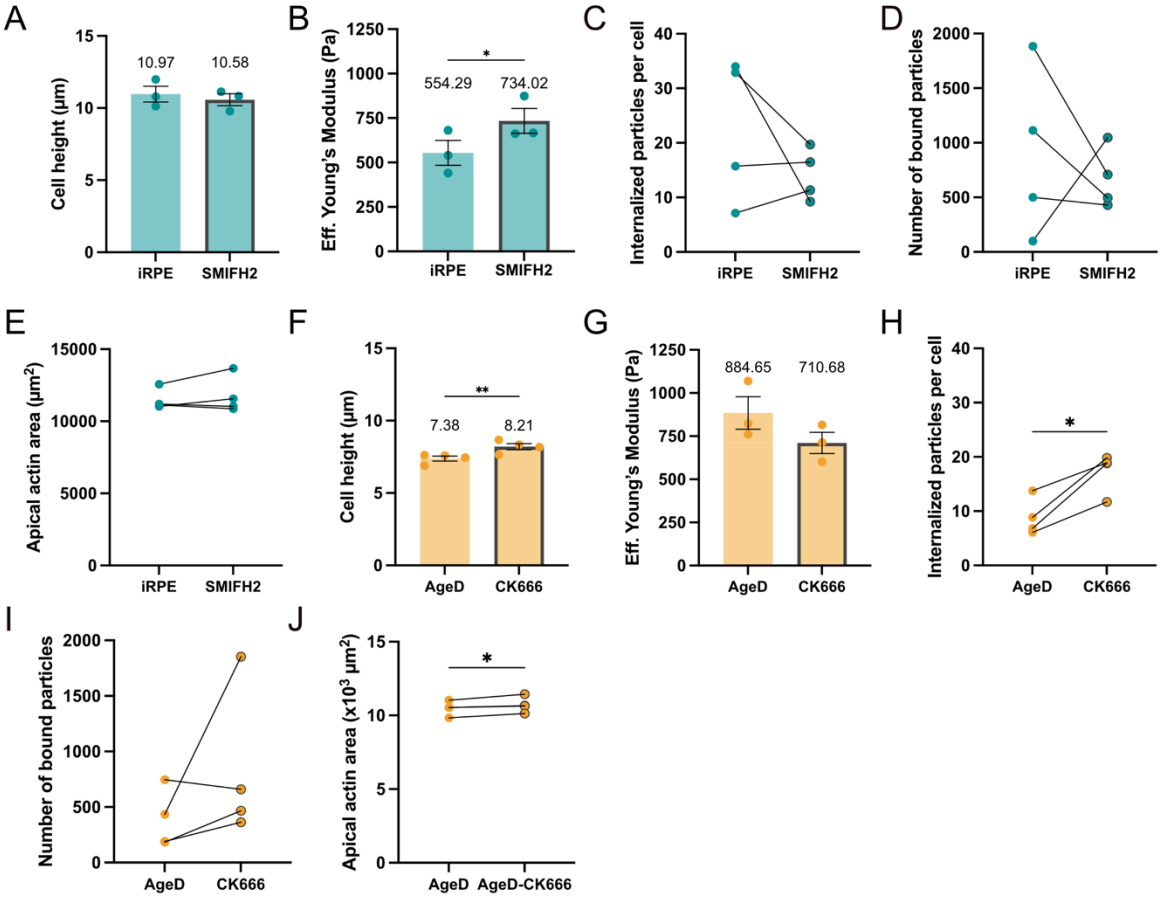

Suppl. figure 8: Nucleator inhibition during photoreceptor phagocytosis. A: Quantification of cell height for iRPE vs SMIFH2-treated iRPE. **B:** Average Effective Young's Modulus, derived from 2.5 µm nanoindentation with a 20 µm spherical tip for iRPE vs SMIFH2-treated iRPE monolayers. **C:** Quantification of the number of internalised photoreceptor particles normalised to cell number for iRPE vs SMIFH2-treated iRPE. **D:** Quantification of the number of bound particles in the field of view for iRPE vs SMIFH2-treated iRPE. **E:** Quantification of apical actin area per field of view during internalisation in iRPE vs SMIFH2-treated iRPE. **F:** Quantification of cell height for AgeD-iRPE vs CK666-treated AgeD-iRPE. **G:** Average Effective Young's Modulus, derived from 2.5 µm nanoindentation with a 20 µm spherical tip for AgeD-iRPE vs CK666-treated AgeD-iRPE. **H:** Quantification of the number of internalised photoreceptor particles normalised to cell number for AgeD-iRPE vs CK666-treated AgeD-iRPE monolayers. **I:** Quantification of the number of bound particles in the field of view for AgeD-iRPE vs CK666-treated AgeD-iRPE. **J:** Quantification of apical actin area per field of view of monolayers during internalisation in AgeD-iRPE vs CK666-treated AgeD-iRPE. Datapoints represent average values (± SEM in case of bar graphs) per experiment originating from 3 to 4 independent experiments. Statistical significance was tested using a paired t-test, where *: $p<0.05$ and **: $p<0.01$.

942 **Supplementary information**

943

944 **Table 1: Antibodies and dyes used for immunofluorescence (IF) or immunoblotting (WB).**

Name	Source	Concentration/Dilution
	Primary antibodies	
Anti phospho-myosin light chain 2 (Ser19)	Cell Signalling, 3671	1:50 (IF); 1:1000 (WB)
Anti vinculin	Sigma, V4139	15 µg/ml (IF)
Anti ezrin	abcam, ab4069	10 µg/ml (IF); 1 µg/ml (WB)
Anti phospho ezrin (Thr567)	Invitrogen, PA5-37763	5 µg/ml (IF); 1 µg/ml (WB)
Anti non muscle myosin heavy chain IIB	BioLegend, 909901	4 µg/ml (IF)
	Secondary antibodies	
AF488 anti mouse IgG (H+L)	Invitrogen, A11001	8 µg/ml (IF)
AF594 anti mouse IgG (H+L)	Invitrogen, A11005	8 µg/ml (IF)
AF594 anti rabbit IgG (H+L)	Invitrogen, A11012	8 µg/ml (IF)
AF647 anti rabbit IgG (H+L)	Jackson/Dianova, 111-605-144	7,5 µg/ml (IF)
AF 488 anti rabbit IgG (H+L)	Jackson/Dianova, 711-546-152	8 µg/ml (IF)
HRP anti rabbit IgG	Abcam, ab99696	1:5000 (WB)
HRP anti mouse IgG (H+L)	Jackson/Dianova, 115-035-003	1:5000 (WB)
	Fluorescent dyes	
Phalloidin-iFluor 488	Abcam, ab176753	1:200 (IF)
Phalloidin-iFluor 647	Abcam, ab176759	1:200 (IF)
Phalloidin AF568	Molecular probes, A12380	1:200 (IF)

945

946 **Videos Legends**

947 **Video 1: On-demand activation of FKBP/casp8 by AP20187 leads to monolayer-scale**
948 **extrusion events.** Live-iRPE monolayer time-lapse expressing FKBP/casp8 (mApple-
949 positive red cells) and labelled with actin dye SiR-Actin (white). Upon the addition of the
950 AP20187 compound, cells are extruded due to apoptosis induction. Extrusion events
951 include neighbouring cells adopting a characteristic rosette-like morphology, while the
952 dying cell is extruded out of the monolayer, forming a bright blob.

953

954 **Video 2: Live-cell time-lapse of iRPE monolayer during nanoindentation.** The SiR-
955 Actin labelled iRPE monolayer is probed by nanoindentation in a matrix scan (left). A
956 zoom-in view (right) reveals the junctional deformation occurring during the
957 measurement.

References

1. J. A. Thomson, On Growth and Form. **100**, 21–22 (1917).

2. P. Ball, *Shapes: Nature's Patterns* (Oxford University Press, USA, 2009).

3. T. Bepler, B. Berger, Learning the protein language: Evolution, structure, and function. *Cell Syst.* **12**, 654-669.e3 (2021).

4. V. Gligorijević, P. D. Renfrew, T. Kosciolek, J. K. Leman, D. Berenberg, T. Vatanen, C. Chandler, B. C. Taylor, I. M. Fisk, H. Vlamakis, R. J. Xavier, R. Knight, K. Cho, R. Bonneau, Structure-based protein function prediction using graph convolutional networks. *Nat. Commun.* **12**, 3168 (2020).

5. J. Yang, A. Griffin, Z. Qiang, J. Ren, Organelle-targeted therapies: a comprehensive review on system design for enabling precision oncology. *Signal Transduct. Target. Ther.* **7**, 379 (2022).

6. B. Glancy, Y. Kim, P. Katti, T. B. Willingham, The Functional Impact of Mitochondrial Structure Across Subcellular Scales. *Front. Physiol.* **11**, 541040 (2020).

7. E. F. Morgan, L. C. Gerstenfeld, Marcus and Feldman's Osteoporosis. 15–35 (2021).

8. G. L. Baum, Z. Cui, D. R. Roalf, R. Ciric, R. F. Betzel, B. Larsen, M. Cieslak, P. A. Cook, C. H. Xia, T. M. Moore, K. Ruparel, D. J. Oathes, A. F. Alexander-Bloch, R. T. Shinohara, A. Raznahan, R. E. Gur, R. C. Gur, D. S. Bassett, T. D. Satterthwaite, Development of structure–function coupling in human brain networks during youth. *Proc. Natl. Acad. Sci.* **117**, 771–778 (2020).

9. C. L. Simpson, D. M. Patel, K. J. Green, Deconstructing the skin: cytoarchitectural determinants of epidermal morphogenesis. *Nat. Rev. Mol. Cell Biol.* **12**, 565–580 (2011).

10. A. A. Anlaş, C. M. Nelson, Tissue mechanics regulates form, function, and dysfunction. *Curr. Opin. Cell Biol.* **54**, 98–105 (2018).

11. N. M. E. Ayad, S. Kaushik, V. M. Weaver, Tissue mechanics, an important regulator of development and disease. *Philosophical Transactions Royal Soc B* **374**, 20180215 (2019).

12. C. Guillot, T. Lecuit, Mechanics of Epithelial Tissue Homeostasis and Morphogenesis. *Science* **340**, 1185–1189 (2013).

13. L. C. Biggs, C. S. Kim, Y. A. Miroshnikova, S. A. Wickström, Mechanical Forces in the Skin: Roles in Tissue Architecture, Stability, and Function. *J. Investig. Dermatol.* **140**, 284–290 (2020).

14. C. F. Guimarães, L. Gasperini, A. P. Marques, R. L. Reis, The stiffness of living tissues and its implications for tissue engineering. *Nat. Rev. Mater.* **5**, 351–370 (2020).

15. P. Gómez-Gálvez, S. Anbari, L. M. Escudero, J. Buceta, Mechanics and self-organization in tissue development. *Semin. Cell Dev. Biol.* **120**, 147–159 (2021).

16. J. F. Eichinger, L. J. Haeusel, D. Paukner, R. C. Aydin, J. D. Humphrey, C. J. Cyron, Mechanical homeostasis in tissue equivalents: a review. *Biomech. Model. Mechanobiol.* **20**, 833–850 (2021).

17. Y. Tamori, W.-M. Deng, Tissue Repair through Cell Competition and Compensatory Cellular Hypertrophy in Postmitotic Epithelia. *Dev. Cell* **25**, 350–363 (2013).

18. L. Campello, N. Singh, J. Advani, A. K. Mondal, X. Corso-Diaz, A. Swaroop, Aging of the Retina: Molecular and Metabolic Turbulences and Potential Interventions. *Annu Rev Vis Sc* **7**, 1–32 (2021).

19. R. D. Terry, R. DeTeresa, L. A. Hansen, Neocortical cell counts in normal human adult aging. *Ann. Neurol.* **21**, 530–539 (1987).

20. S. H. Freeman, R. Kandel, L. Cruz, A. Rozkalne, K. Newell, M. P. Frosch, E. T. Hedley-Whyte, J. J. Locascio, L. A. Lipsitz, B. T. Hyman, Preservation of Neuronal Number Despite Age-Related Cortical Brain Atrophy in Elderly Subjects Without Alzheimer Disease. *J. Neuropathol. Exp. Neurol.* **67**, 1205–1212 (2008).

21. T. Piskova, A. N. Kozyrina, J. Di Russo, Mechanobiological implications of age-related remodelling in the outer retina. *Biomater. Adv.* **147**, 213343 (2023).

22. J. R. Sparrrow, D. Hicks, C. P. Hamel, The Retinal Pigment Epithelium in Health and Disease. *Curr. Mol. Med.* **10**, 802–823 (2010).

23. S. Panda-Jonas, J. B. JONAS, M. JAKOBCZYK-ZMIJA, Retinal Pigment Epithelial Cell Count, Distribution, and Correlations in Normal Human Eyes. *Am. J. Ophthalmol.* **121**, 181–189 (1996).

24. S. K. Bhatia, A. Rashid, M. A. Chrenek, Q. Zhang, B. B. Bruce, M. Klein, J. H. Boatright, Y. Jiang, H. E. Grossniklaus, J. M. Nickerson, Analysis of RPE morphometry in human eyes. *Mol Vis* **22**, 898–916 (2016).

25. L. V. D. Priore, Y.-H. Kuo, T. H. Tezel, Age-related changes in human RPE cell density and apoptosis proportion in situ. *Invest Ophth Vis Sci* **43**, 3312–8 (2002).

26. M. L. Katz, W. G. Robison, Age-related changes in the retinal pigment epithelium of pigmented rats. *Exp Eye Res* **38**, 137–151 (1984).

27. I.-S. Tarau, A. Berlin, C. A. Curcio, T. Ach, The Cytoskeleton of the Retinal Pigment Epithelium: from Normal Aging to Age-Related Macular Degeneration. *Int J Mol Sci* **20**, 3578 (2019).

1025 28. Y. L. Lai, M. W. Rana, A Study of Photoreceptor–Retinal Pigment Epithelium Complex:
1026 Age-Related Changes in Monkeys. *P Soc Exp Biol Med* **181**, 371–381 (1986).

1027 29. G. Inana, C. Murat, W. An, X. Yao, I. R. Harris, J. Cao, RPE phagocytic function declines
1028 in age-related macular degeneration and is rescued by human umbilical tissue derived
1029 cells. *J Transl Med* **16**, 63 (2018).

1030 30. J. Y. W. Ma, U. Greferath, J. H. C. Wong, L. J. Fothergill, A. I. Jobling, K. A. Vessey, E. L.
1031 Fletcher, Aging induces cell loss and a decline in phagosome processing in the mouse
1032 retinal pigment epithelium. *Neurobiol. Aging* **128**, 1–16 (2023).

1033 31. N. Diwanji, A. Bergmann, Two Sides of the Same Coin - Compensatory Proliferation in
1034 Regeneration and Cancer. *Adv. Exp. Med. Biol.* **1167**, 65–85 (2019).

1035 32. C. Brandl, S. J. Zimmermann, V. M. Milenkovic, S. M. G. Rosendahl, F. Grassmann, A.
1036 Milenkovic, U. Hehr, M. Federlin, C. H. Wetzel, H. Helbig, B. H. F. Weber, In-Depth
1037 Characterisation of Retinal Pigment Epithelium (RPE) Cells Derived from Human Induced
1038 Pluripotent Stem Cells (hiPSC). *NeuroMolecular Med.* **16**, 551–564 (2014).

1039 33. K. J. Miyagishima, Q. Wan, B. Corneo, R. Sharma, M. R. Lotfi, N. C. Boles, F. Hua, A.
1040 Maminishkis, C. Zhang, T. Blenkinsop, V. Khristov, B. S. Jha, O. S. Memon, S. D'Souza, S.
1041 Temple, S. S. Miller, K. Bharti, In Pursuit of Authenticity: Induced Pluripotent Stem Cell-
1042 Derived Retinal Pigment Epithelium for Clinical Applications. *STEM CELLS Transl. Med.* **5**,
1043 1562–1574 (2016).

1044 34. A. N. Kozyrina, T. Piskova, F. Semeraro, I. C. Doolaar, T. Prapty, T. Haraszti, M. Hubert,
1045 R. Windoffer, R. E. Leube, A.-S. Smith, J. Di Russo, Laminin-defined mechanical status
1046 modulates retinal pigment epithelium phagocytosis. *EMBO Rep.*, 1–27 (2025).

1047 35. A. Oberst, C. Pop, A. G. Tremblay, V. Blais, J.-B. Denault, G. S. Salvesen, D. R. Green,
1048 Inducible Dimerization and Inducible Cleavage Reveal a Requirement for Both Processes
1049 in Caspase-8 Activation*. *J. Biol. Chem.* **285**, 16632–16642 (2010).

1050 36. F. Ko, P. J. Foster, N. G. Strouthidis, Y. Shweikh, Q. Yang, C. A. Reisman, Z. A. Muthy,
1051 U. Chakravarthy, A. J. Lotery, P. A. Keane, A. Tufail, C. M. Grossi, P. J. Patel, U. B. E. V.
1052 Consortium, Associations with Retinal Pigment Epithelium Thickness Measures in a
1053 Large Cohort Results from the UK Biobank. *Ophthalmology* **124**, 105–117 (2017).

1054 37. V. L. Bonilha, M. E. Rayborn, I. Saotome, A. I. McClatchey, J. G. Hollyfield, Microvilli
1055 defects in retinas of ezrin knockout mice. *Exp. Eye Res.* **82**, 720–729 (2006).

1056 38. T. Kivelä, J. Jääskeläinen, A. Vaheri, O. Carpén, Ezrin, a membrane-organizing protein,
1057 as a polarization marker of the retinal pigment epithelium in vertebrates. *Cell Tissue Res.*
1058 **301**, 217–223 (2000).

1059 39. V. L. Bonilha, S. C. Finnemann, E. Rodriguez-Boulan, Ezrin Promotes Morphogenesis
1060 of Apical Microvilli and Basal Infoldings in Retinal Pigment Epithelium. *J. Cell Biol.* **147**,
1061 1533–1548 (1999).

1062 40. B. T. Fievet, A. Gautreau, C. Roy, L. D. Maestro, P. Mangeat, D. Louvard, M. Arpin,
1063 Phosphoinositide binding and phosphorylation act sequentially in the activation
1064 mechanism of ezrin. *J. Cell Biol.* **164**, 653–659 (2004).

1065 41. R. Tixeira, S. Caruso, S. Paone, A. A. Baxter, G. K. Atkin-Smith, M. D. Hulett, I. K. H.
1066 Poon, Defining the morphologic features and products of cell disassembly during
1067 apoptosis. *Apoptosis* **22**, 475–477 (2017).

1068 42. C. Zihni, Phagocytosis by the retinal pigment epithelium: New insights into polarized
1069 cell mechanics. *BioEssays* **47**, e2300197 (2025).

1070 43. A. Umapathy, G. Torten, A. E. Paniagua, J. Chung, M. Tomlinson, C. Lim, D. S.
1071 Williams, Spatiotemporal Live-Cell Analysis of Photoreceptor Outer Segment Membrane
1072 Ingestion by the Retinal Pigment Epithelium Reveals Actin-Regulated Scission. *J.*
1073 *Neurosci.* **43**, 2653–2664 (2023).

1074 44. C. Müller, C. Charniga, S. Temple, S. C. Finnemann, Quantified F-Actin Morphology Is
1075 Predictive of Phagocytic Capacity of Stem Cell-Derived Retinal Pigment Epithelium. *Stem*
1076 *Cell Rep* **10**, 1075–1087 (2018).

1077 45. J. Y. W. Ma, U. Greferath, J. H. C. Wong, L. J. Fothergill, A. I. Jobling, K. A. Vessey, E. L.
1078 Fletcher, Aging induces cell loss and a decline in phagosome processing in the mouse
1079 retinal pigment epithelium. *Neurobiol. Aging* **128**, 1–16 (2023).

1080 46. W. Kwon, S. A. Freeman, Phagocytosis by the Retinal Pigment Epithelium:
1081 Recognition, Resolution, Recycling. *Front Immunol* **11**, 604205 (2020).

1082 47. E. N. Olson, A. Nordheim, Linking actin dynamics and gene transcription to drive
1083 cellular motile functions. *Nat. Rev. Mol. Cell Biol.* **11**, 353–365 (2010).

1084 48. H. Cai, M. A. Fields, R. Hoshino, L. V. D. Priore, Effects of Aging and Anatomic Location
1085 on Gene Expression in Human Retina. *Front. Aging Neurosci.* **4**, 8 (2012).

1086 49. J. M. Butler, W. Supharattanasitthi, Y. C. Yang, L. Paraoan, RNA-seq analysis of ageing
1087 human retinal pigment epithelium: Unexpected up-regulation of visual cycle gene
1088 transcription. *J. Cell. Mol. Med.* **25**, 5572–5585 (2021).

1089 50. O. Chaudhuri, Viscoelastic hydrogels for 3D cell culture. *Biomater. Sci.* **5**, 1480–1490
1090 (2017).

1091 51. M. Nagayama, H. Haga, M. Takahashi, T. Saitoh, K. Kawabata, Contribution of cellular
1092 contractility to spatial and temporal variations in cellular stiffness. *Exp. Cell Res.* **300**,
1093 396–405 (2004).

1094 52. N. Wang, I. M. Tolić-Nørrelykke, J. Chen, S. M. Mijailovich, J. P. Butler, J. J. Fredberg,
1095 D. Stamenović, Cell prestress. I. Stiffness and prestress are closely associated in
1096 adherent contractile cells. *Am. J. Physiol.-Cell Physiol.* **282**, C606–C616 (2002).

1097 53. T. Watanabe, H. Hosoya, S. Yonemura, Regulation of Myosin II Dynamics by
1098 Phosphorylation and Dephosphorylation of Its Light Chain in Epithelial Cells. *Mol. Biol.*
1099 *Cell* **18**, 605–616 (2007).

1100 54. J. M. Leerberg, A. S. Yap, Vinculin, cadherin mechanotransduction and homeostasis
1101 of cell–cell junctions. *Protoplasma* **250**, 817–829 (2013).

1102 55. B. R. Brückner, A. Janshoff, Importance of integrity of cell-cell junctions for the
1103 mechanics of confluent MDCK II cells. *Sci. Rep.* **8**, 14117 (2018).

1104 56. R. Prevedel, A. Diz-Muñoz, G. Ruocco, G. Antonacci, Brillouin microscopy: an
1105 emerging tool for mechanobiology. *Nat Methods* **16**, 969–977 (2019).

1106 57. P. Chugh, A. G. Clark, M. B. Smith, D. A. D. Cassani, K. Dierkes, A. Ragab, P. P. Roux,
1107 G. Charras, G. Salbreux, E. K. Paluch, Actin cortex architecture regulates cell surface
1108 tension. *Nat. cell Biol.* **19**, 689–697 (2017).

1109 58. S. Y. Lee, T. Fujioka, M. Osuga, T. Nishimura, S. Suetsugu, Plasma Membrane Shaping.
1110 245–263 (2023).

1111 59. B. Hetrick, M. S. Han, L. A. Helgeson, B. J. Nolen, Small Molecules CK-666 and CK-
1112 869 Inhibit Actin-Related Protein 2/3 Complex by Blocking an Activating Conformational
1113 Change. *Chem. Biol.* **20**, 701–712 (2013).

1114 60. S. A. Rizvi, E. M. Neidt, J. Cui, Z. Feiger, C. T. Skau, M. L. Gardel, S. A. Kozmin, D. R.
1115 Kovar, Identification and Characterization of a Small Molecule Inhibitor of Formin-
1116 Mediated Actin Assembly. *Chem. Biol.* **16**, 1158–1168 (2009).

1117 61. C. López-Otín, M. A. Blasco, L. Partridge, M. Serrano, G. Kroemer, Hallmarks of aging:
1118 An expanding universe. *Cell* **186**, 243–278 (2023).

1119 62. T. Schmauck-Medina, A. Molière, S. Lautrup, J. Zhang, S. Chlopicki, H. B. Madsen, S.
1120 Cao, C. Soendenbroe, E. Mansell, M. B. Vestergaard, Z. Li, Y. Shiloh, P. L. Opresko, J.-M.
1121 Egly, T. Kirkwood, E. Verdin, V. A. Bohr, L. S. Cox, T. Stevnsner, L. J. Rasmussen, E. F. Fang,
1122 New hallmarks of ageing: a 2022 Copenhagen ageing meeting summary. *Aging* **14**, 6829–
1123 6839 (2022).

1124 63. L. C. D. Pomatto, K. J. A. Davies, The role of declining adaptive homeostasis in ageing.
1125 *J. Physiol.* **595**, 7275–7309 (2017).

1126 64. D. Cornacchia, L. Studer, Back and forth in time: Directing age in iPSC-derived
1127 lineages. *Brain Res.* **1656**, 14–26 (2017).

1128 65. V. L. Bonilha, Age and disease-related structural changes in the retinal pigment
1129 epithelium. *Clin Ophthalmol Auckl N Z* **2**, 413–424 (2008).

1130 66. M. Chen, D. Rajapakse, M. Fraczek, C. Luo, J. V. Forrester, H. Xu, Retinal pigment
1131 epithelial cell multinucleation in the aging eye – a mechanism to repair damage and
1132 maintain homoeostasis. *Aging Cell* **15**, 436–445 (2016).

1133 67. Y. Tamori, W.-M. Deng, Compensatory cellular hypertrophy: the other strategy for
1134 tissue homeostasis. *Trends Cell Biol* **24**, 230–237 (2014).

1135 68. J. F. E. Bodenschatz, K. Ajmail, M. Skamrahl, M. Vache, J. Gottwald, S. Nehls, A.
1136 Janshoff, Epithelial cells sacrifice excess area to preserve fluidity in response to external
1137 mechanical stress. *Commun. Biol.* **5**, 855 (2022).

1138 69. L. Figard, M. Wang, L. Zheng, I. Golding, A. M. Sokac, Membrane Supply and Demand
1139 Regulates F-Actin in a Cell Surface Reservoir. *Dev. Cell* **37**, 267–278 (2016).

1140 70. X. Trepat, M. Grabulosa, F. Puig, G. N. Maksym, D. Navajas, R. Farré, Viscoelasticity
1141 of human alveolar epithelial cells subjected to stretch. *Am. J. Physiol.-Lung Cell. Mol.*
1142 *Physiol.* **287**, L1025–L1034 (2004).

1143 71. I. Sokolov, S. Iyer, C. D. Woodworth, Recovery of elasticity of aged human epithelial
1144 cells in vitro. *Nanomed.: Nanotechnol., Biol. Med.* **2**, 31–36 (2006).

1145 72. T. Morris, E. Sue, C. Geniesse, W. M. Brieher, V. W. Tang, Synaptopodin stress fiber
1146 and contractomere at the epithelial junction. *J. Cell Biol.* **221**, e202011162 (2022).

1147 73. J. M. López-Gay, H. Nunley, M. Spencer, F. di Pietro, B. Guirao, F. Bosveld, O. Markova,
1148 I. Gaugue, S. Pelletier, D. K. Lubensky, Y. Bellaïche, Apical stress fibers enable a scaling
1149 between cell mechanical response and area in epithelial tissue. *Science* **370**, eabb2169
1150 (2020).

1151 74. J. L. Bays, H. K. Campbell, C. Heidema, M. Sebbagh, K. A. DeMali, Linking E-cadherin
1152 mechanotransduction to cell metabolism through force-mediated activation of AMPK.
1153 *Nat. Cell Biol.* **19**, 724–731 (2017).

1154 75. F. Geisler, R. A. Coch, C. Richardson, M. Goldberg, C. Bevilacqua, R. Prevedel, R. E.
1155 Leube, Intestinal intermediate filament polypeptides in C. elegans: Common and
1156 isotype-specific contributions to intestinal ultrastructure and function. *Sci. Rep.* **10**, 3142
1157 (2020).

1158 76. P. Zhang, T. N. Medwig-Kinney, B. Goldstein, Architecture of the cortical actomyosin
1159 network driving apical constriction in C. elegans. *J. Cell Biol.* **222**, e202302102 (2023).

1160 77. B. R. Brückner, A. Pietuch, S. Nehls, J. Rother, A. Janshoff, Ezrin is a Major Regulator
1161 of Membrane Tension in Epithelial Cells. *Sci. Rep.* **5**, 14700 (2015).

1162 78. K. Goodwin, E. E. Lostchuck, K. M. L. Cramb, T. Zulueta-Coarasa, R. Fernandez-
1163 Gonzalez, G. Tanentzapf, Cell–cell and cell–extracellular matrix adhesions cooperate to
1164 organize actomyosin networks and maintain force transmission during dorsal closure.
1165 *Mol. Biol. Cell* **28**, 1301–1310 (2017).

1166 79. V. Maruthamuthu, B. Sabass, U. S. Schwarz, M. L. Gardel, Cell-ECM traction force
1167 modulates endogenous tension at cell–cell contacts. *Proc National Acad Sci* **108**, 4708–
1168 4713 (2011).

80. A. Valencia-Expósito, N. Khalilgharibi, A. M.-A. Millán, Y. Mao, M. D. Martín-Bermudo, Local weakening of cell-extracellular matrix adhesion triggers basal epithelial tissue folding. *EMBO J.* **44**, 2002–2024 (2025).

81. D. Vorselen, R. L. D. Labitigan, J. A. Theriot, A mechanical perspective on phagocytic cup formation. *Curr Opin Cell Biol* **66**, 112–122 (2020).

82. E. Hoijman, H.-M. Häkkinen, Q. Tolosa-Ramon, S. Jiménez-Delgado, C. Wyatt, M. Miret-Cuesta, M. Irimia, A. Callan-Jones, S. Wieser, V. Ruprecht, Cooperative epithelial phagocytosis enables error correction in the early embryo. *Nature* **590**, 618–623 (2021).

83. J. X. H. Li, V. W. Tang, W. M. Brieher, Actin protrusions push at apical junctions to maintain E-cadherin adhesion. *Proc. Natl. Acad. Sci.* **117**, 432–438 (2020).

84. Y. Nishimura, S. Shi, F. Zhang, R. Liu, Y. Takagi, A. D. Bershadsky, V. Viasnoff, J. R. Sellers, The Formin Inhibitor, SMIFH2, Inhibits Members of the Myosin Superfamily. *J. Cell Sci.* **134**, jcs.253708 (2021).

85. H. Gao, J. G. Hollyfield, Aging of the human retina. Differential loss of neurons and retinal pigment epithelial cells. *Invest Ophth Vis Sci* **33**, 1–17 (1992).

86. C. A. Curcio, C. L. Millican, K. A. Allen, R. E. Kalina, Aging of the human photoreceptor mosaic: evidence for selective vulnerability of rods in central retina. *Investig. Ophthalmol. Vis. Sci.* **34**, 3278–96 (1993).

87. C. A. Curcio, D. N. Drucker, Retinal ganglion cells in Alzheimer's disease and aging. *Ann. Neurol.* **33**, 248–257 (1993).

88. K. Eliasieh, L. C. Liets, L. M. Chalupa, Cellular Reorganization in the Human Retina during Normal Aging. *Investig. Opthalmology Vis. Sci.* **48**, 2824 (2007).

89. J. R. Tse, A. J. Engler, Preparation of Hydrogel Substrates with Tunable Mechanical Properties. *Curr. Protoc. Cell Biol.* **47**, 10.16.1-10.16.16 (2010).

90. L. Przybyla, J. N. Lakins, R. Sunyer, X. Trepat, V. M. Weaver, Monitoring developmental force distributions in reconstituted embryonic epithelia. *Methods* **94**, 101–113 (2016).

91. C. Parinot, Q. Rieu, J. Chatagnon, S. C. Finnemann, E. F. Nandrot, Large-Scale Purification of Porcine or Bovine Photoreceptor Outer Segments for Phagocytosis Assays on Retinal Pigment Epithelial Cells. *J. Vis. Exp.*, doi: 10.3791/52100 (2014).

92. J. Schindelin, I. Arganda-Carreras, E. Frise, V. Kaynig, M. Longair, T. Pietzsch, S. Preibisch, C. Rueden, S. Saalfeld, B. Schmid, J.-Y. Tinevez, D. J. White, V. Hartenstein, K. Eliceiri, P. Tomancak, A. Cardona, Fiji: an open-source platform for biological-image analysis. *Nat. Methods* **9**, 676–682 (2012).

93. P. A. Ewels, A. Peltzer, S. Fillinger, H. Patel, J. Alneberg, A. Wilm, M. U. Garcia, P. D. Tommaso, S. Nahnsen, The nf-core framework for community-curated bioinformatics pipelines. *Nat. Biotechnol.* **38**, 276–278 (2020).

1205 94. P. D. Tommaso, M. Chatzou, E. W. Floden, P. P. Barja, E. Palumbo, C. Notredame,
1206 Nextflow enables reproducible computational workflows. *Nat. Biotechnol.* **35**, 316–319
1207 (2017).

1208 95. M. I. Love, W. Huber, S. Anders, Moderated estimation of fold change and dispersion
1209 for RNA-seq data with DESeq2. *Genome Biol.* **15**, 550 (2014).

1210 96. R. Kolde, *Pheatmap: Pretty Heatmaps* (2018;
1211 https://github.com/raivokolde/pheatmap).

1212 97. U. Raudvere, L. Kolberg, I. Kuzmin, T. Arak, P. Adler, H. Peterson, J. Vilo, g:Profiler: a
1213 web server for functional enrichment analysis and conversions of gene lists (2019
1214 update). *Nucleic Acids Res.* **47**, W191–W198 (2019).

1215 98. K. A. Janes, An analysis of critical factors for quantitative immunoblotting. *Sci. Signal.*
1216 **8**, rs2 (2015).

1217 99. U. K. LAEMMLI, Cleavage of Structural Proteins during the Assembly of the Head of
1218 Bacteriophage T4. *Nature* **227**, 680–685 (1970).

1219 100. J. L. Brunelle, R. Green, One-dimensional SDS-polyacrylamide gel electrophoresis
1220 (1D SDS-PAGE). *Methods Enzym.* **541**, 151–9 (2014).

1221 101. C. Stringer, T. Wang, M. Michaelos, M. Pachitariu, Cellpose: a generalist algorithm
1222 for cellular segmentation. *Nat. Methods* **18**, 100–106 (2021).

1223 102. D. Bi, J. H. Lopez, J. M. Schwarz, M. L. Manning, A density-independent rigidity
1224 transition in biological tissues. *Nat. Phys.* **11**, 1074–1079 (2015).

1225 103. J.-A. Park, J. H. Kim, D. Bi, J. A. Mitchel, N. T. Qazvini, K. Tantisira, C. Y. Park, M.
1226 McGill, S.-H. Kim, B. Gweon, J. Notbohm, R. S. Jr, S. Burger, S. H. Randell, A. T. Kho, D. T.
1227 Tambe, C. Hardin, S. A. Shore, E. Israel, D. A. Weitz, D. J. Tschumperlin, E. P. Henske, S.
1228 T. Weiss, M. L. Manning, J. P. Butler, J. M. Drazen, J. J. Fredberg, Unjamming and cell shape
1229 in the asthmatic airway epithelium. *Nat. Mater.* **14**, 1040–1048 (2015).

1230

1231

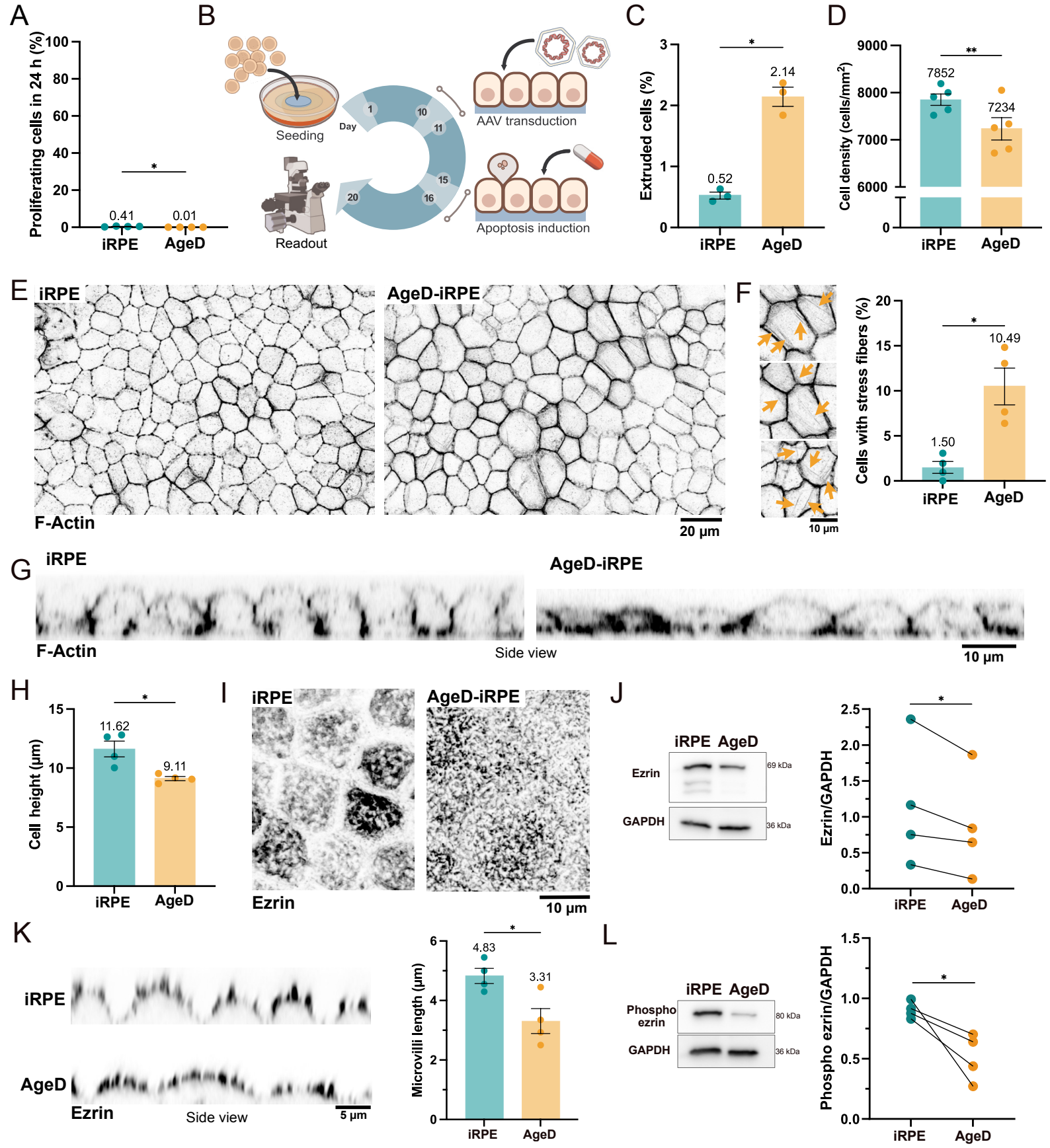
A
Proliferating cells in 24 h (%)
100
80
60
40
20
0
*
0.41
0.01
iRPE
AgeD
B
Seeding
Day
1
10
11
15
16
20
AAV transduction
Apoptosis induction
Readout
C
Extruded cells (%)
3
2
1
0
*
2.14
0.52
iRPE
AgeD
D
Cell density (cells/mm²)
9000
8000
7000
6000
0
**
7852
7234
iRPE
AgeD
E
iRPE
AgeD-iRPE
F-Actin
20 µm
F
10 µm
Cells with stress fibers (%)
20
15
10
5
0
*
10.49
1.50
iRPE
AgeD
G
iRPE
AgeD-iRPE
F-Actin
Side view
10 µm
H
Cell height (µm)
15
10
5
0
*
11.62
9.11
iRPE
AgeD
I
iRPE
AgeD-iRPE
Ezrin
10 µm
J
iRPE AgeD
Ezrin
69 kDa
GAPDH
36 kDa
Ezrin/GAPDH
2.5
2.0
1.5
1.0
0.5
0.0
*
iRPE
AgeD
K
iRPE
AgeD
Ezrin
Side view
5 µm
Microvilli length (µm)
6
4
2
0
*
4.83
3.31
iRPE
AgeD
L
iRPE AgeD
Phospho ezrin
80 kDa
GAPDH
36 kDa
Phospho ezrin/GAPDH
1.5
1.0
0.5
0.0
*
iRPE
AgeD

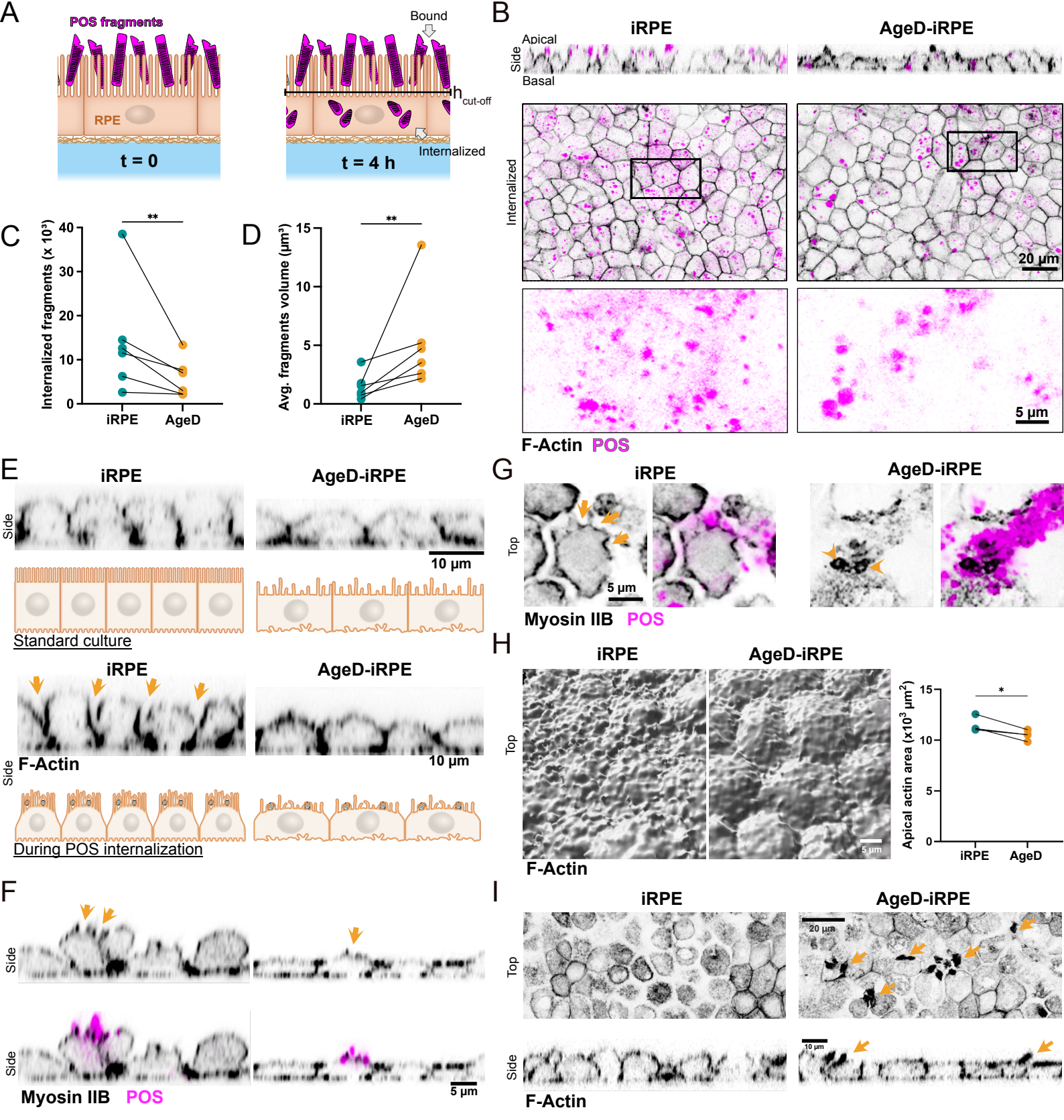
A
POS fragments
RPE
t = 0
Bound
h cut-off
Internalized
t = 4 h
B
iRPE
AgeD-iRPE
Apical
Side
Basal
Internalized
20 µm
5 µm
F-Actin POS
C
Internalized fragments (x 10³)
iRPE
AgeD
D
Avg. fragments volume (µm³)
iRPE
AgeD
E
iRPE
AgeD-iRPE
Side
10 µm
Standard culture
iRPE
AgeD-iRPE
F-Actin
Side
10 µm
During POS internalization
F
Side
Side
Myosin IIB POS
5 µm
G
iRPE
AgeD-iRPE
Top
5 µm
Myosin IIB POS
H
iRPE
AgeD-iRPE
Top
5 µm
F-Actin
Apical actin area (x10³ µm²)
iRPE
AgeD
I
iRPE
AgeD-iRPE
Top
20 µm
Side
10 µm
F-Actin

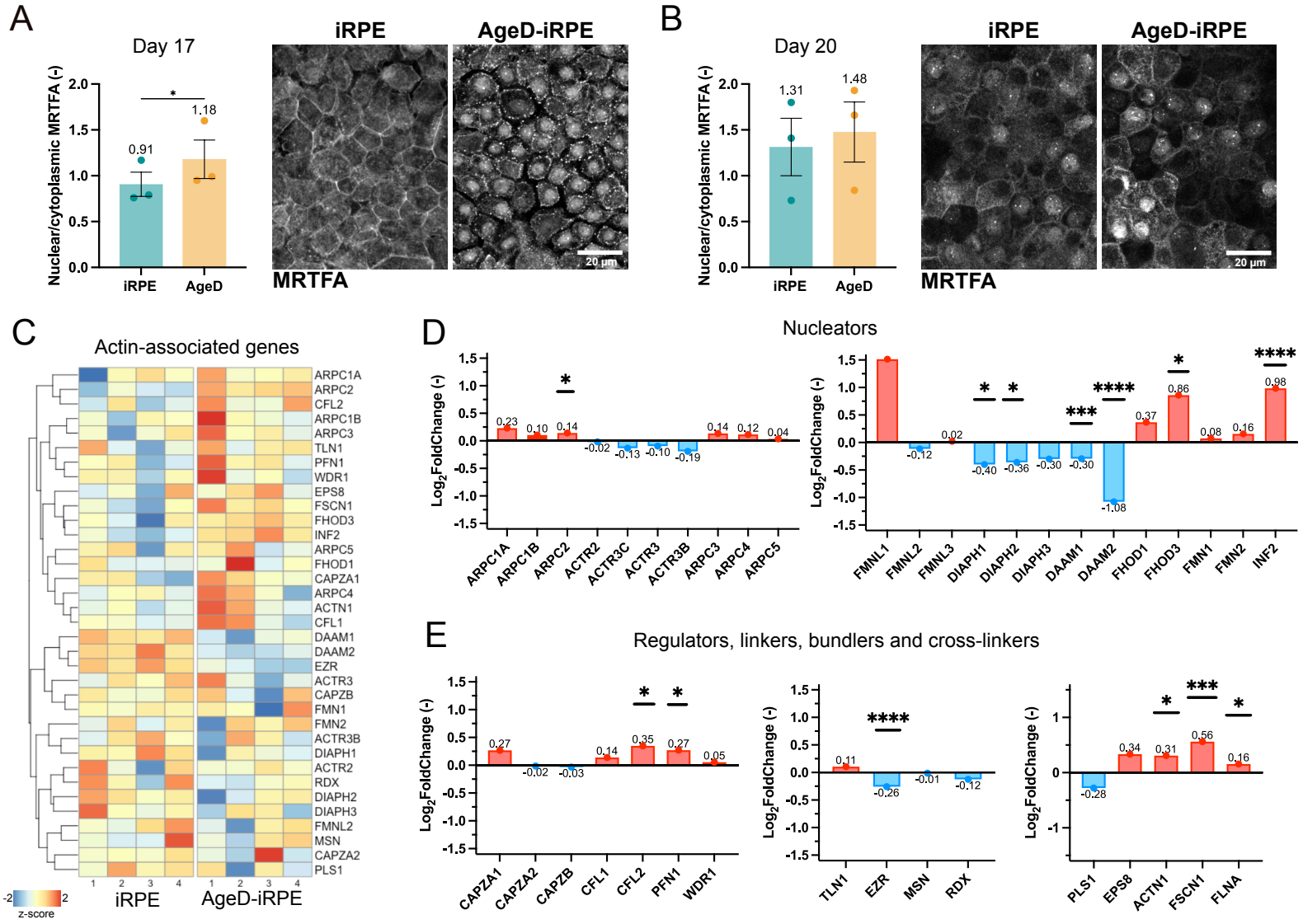
A
Day 17
iRPE
AgeD-iRPE
Nuclear/cytoplasmic MRTFA (-)
2.0
1.5
1.0
0.5
0.0
*
0.91
1.18
iRPE
AgeD
MRTFA
20 µm
B
Day 20
iRPE
AgeD-iRPE
Nuclear/cytoplasmic MRTFA (-)
1.31
1.48
iRPE
AgeD
MRTFA
20 µm
C
Actin-associated genes
ARPC1A
ARPC2
CFL2
ARPC1B
ARPC3
TLN1
PFN1
WDR1
EPS8
FSCN1
FHOD3
INF2
ARPC5
FHOD1
CAPZA1
ARPC4
ACTN1
CFL1
DAAM1
DAAM2
EZR
ACTR3
CAPZB
FMN1
FMN2
ACTR3B
DIAPH1
ACTR2
RDX
DIAPH2
DIAPH3
FMNL2
MSN
CAPZA2
PLS1
1 2 3 4
iRPE
1 2 3 4
AgeD-iRPE
-2
2
z-score
D
Nucleators
Log2FoldChange (-)
1.5
1.0
0.5
0.0
-0.5
-1.0
-1.5
*
0.23
0.10
0.14
-0.02
-0.13
-0.10
-0.19
0.14
0.12
0.04
ARPC1A
ARPC1B
ARPC2
ACTR2
ACTR3C
ACTR3
ACTR3B
ARPC3
ARPC4
ARPC5
*
*
***
****
*
****
0.02
-0.12
-0.40
-0.36
-0.30
-0.30
-1.08
0.37
0.86
0.08
0.16
0.98
FMNL1
FMNL2
FMNL3
DIAPH1
DIAPH2
DIAPH3
DAAM1
DAAM2
FHOD1
FHOD3
FMN1
FMN2
INF2
E
Regulators, linkers, bundlers and cross-linkers
Log2FoldChange (-)
*
*
0.27
-0.02
-0.03
0.14
0.35
0.27
0.05
CAPZA1
CAPZA2
CAPZB
CFL1
CFL2
PFN1
WDR1
****
0.11
-0.26
-0.01
-0.12
TLN1
EZR
MSN
RDX
*
***
*
-0.28
0.34
0.31
0.56
0.16
PLS1
EPS8
ACTN1
FSCN1
FLNA

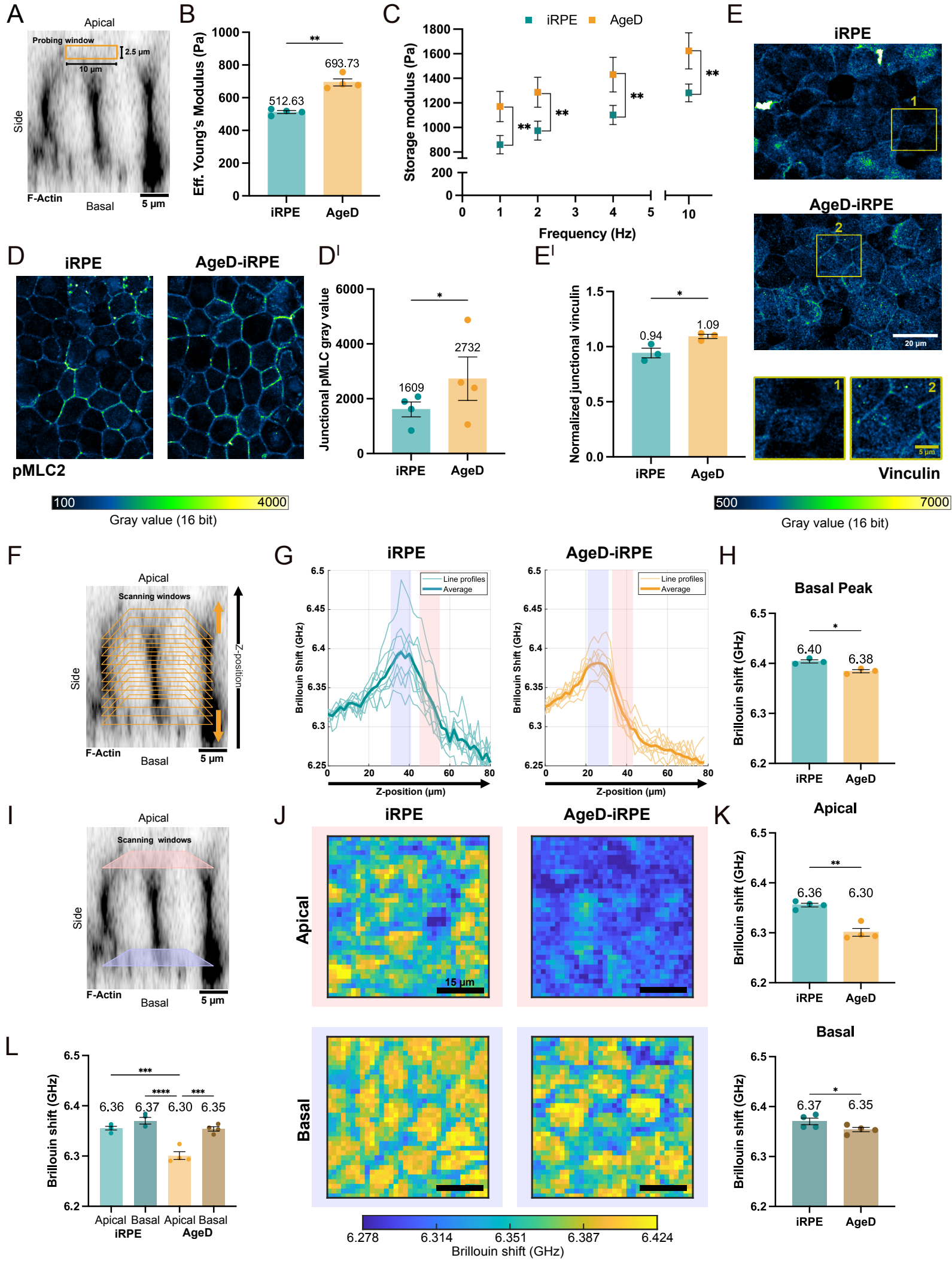
A
Apical
Probing window
2.5 µm
10 µm
Side
F-Actin
Basal
5 µm
B
Eff. Young's Modulus (Pa)
1000
800
600
400
200
0
**
512.63
693.73
iRPE
AgeD
C
iRPE
AgeD
Storage modulus (Pa)
1800
1600
1400
1200
1000
800
200
0
**
**
**
**
0
1
2
3
4
5
10
Frequency (Hz)
E
iRPE
1
AgeD-iRPE
2
20 µm
1
2
5 µm
Vinculin
500
7000
Gray value (16 bit)
D
iRPE
AgeD-iRPE
pMLC2
100
4000
Gray value (16 bit)
D'
Junctional pMLC gray value
6000
4000
2000
0
*
1609
2732
iRPE
AgeD
E'
Normalized junctional vinculin
1.5
1.0
0.5
0.0
*
0.94
1.09
iRPE
AgeD
F
Apical
Scanning windows
Side
Z-position
F-Actin
Basal
5 µm
G
iRPE
AgeD-iRPE
Line profiles
Average
Brillouin Shift (GHz)
6.5
6.45
6.4
6.35
6.3
6.25
0
20
40
60
80
Z-position (µm)
H
Basal Peak
Brillouin shift (GHz)
6.5
6.4
6.3
6.2
*
6.40
6.38
iRPE
AgeD
I
Apical
Scanning windows
Side
F-Actin
Basal
5 µm
J
iRPE
AgeD-iRPE
Apical
15 µm
Basal
6.278
6.314
6.351
6.387
6.424
Brillouin shift (GHz)
K
Apical
Brillouin shift (GHz)
6.5
6.4
6.3
6.2
**
6.36
6.30
iRPE
AgeD
Basal
Brillouin shift (GHz)
6.5
6.4
6.3
6.2
*
6.37
6.35
iRPE
AgeD
L
Brillouin shift (GHz)
6.5
6.4
6.3
6.2
***
****
***
6.36
6.37
6.30
6.35
Apical
Basal
Apical
Basal
iRPE
AgeD

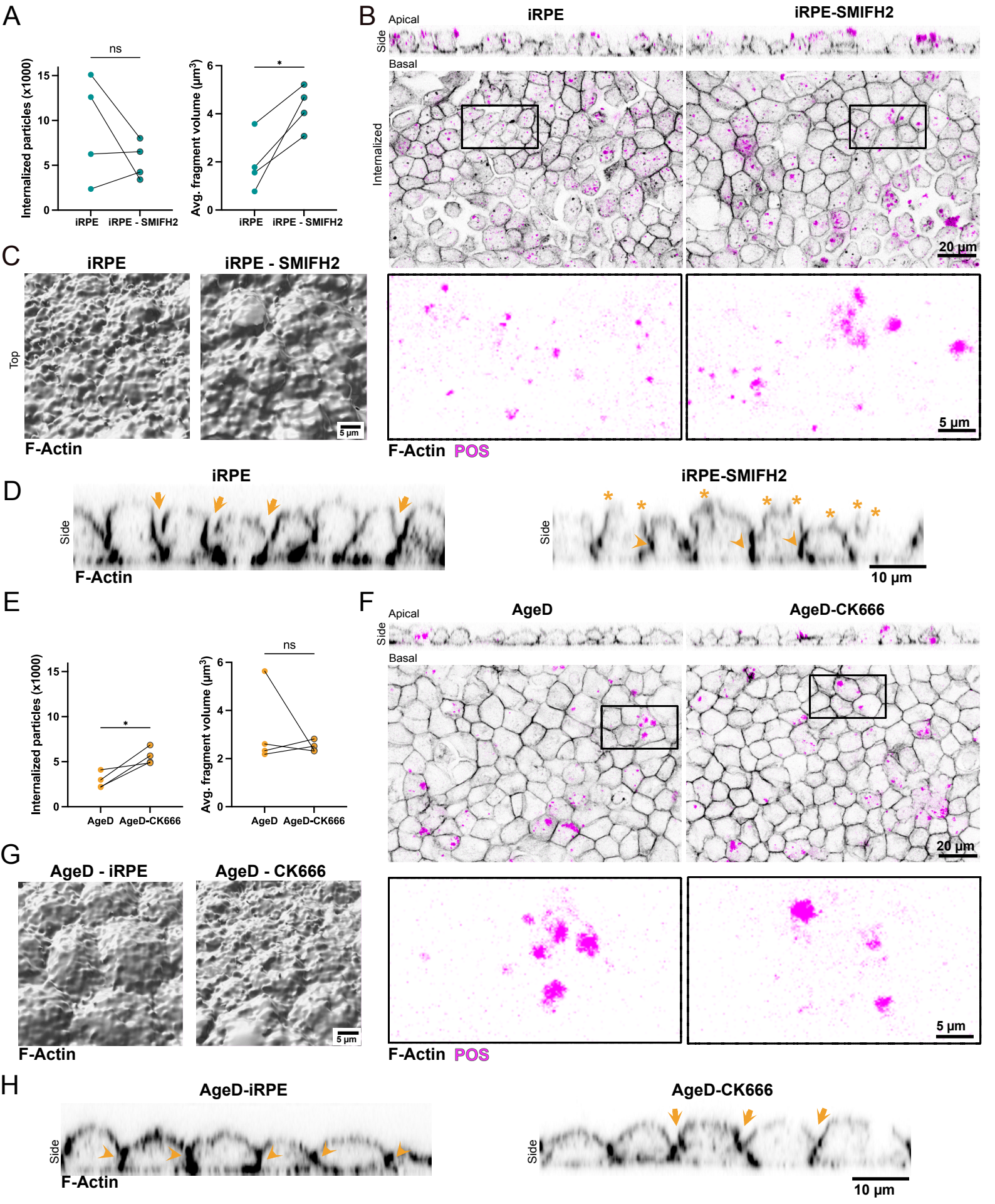
A
ns
Internalized particles (x1000)
15
10
5
0
iRPE
iRPE - SMIFH2
*
Avg. fragment volume (µm³)
6
4
2
0
iRPE
iRPE - SMIFH2
B
Apical
iRPE
iRPE-SMIFH2
Side
Basal
Internalized
20 µm
5 µm
F-Actin POS
C
iRPE
iRPE - SMIFH2
Top
5 µm
F-Actin
D
iRPE
Side
F-Actin
iRPE-SMIFH2
Side
10 µm
E
Internalized particles (x1000)
15
10
5
0
*
AgeD
AgeD-CK666
ns
Avg. fragment volume (µm³)
6
4
2
0
AgeD
AgeD-CK666
F
Apical
AgeD
AgeD-CK666
Side
Basal
20 µm
5 µm
F-Actin POS
G
AgeD - iRPE
AgeD - CK666
5 µm
F-Actin
H
AgeD-iRPE
Side
F-Actin
AgeD-CK666
Side
10 µm

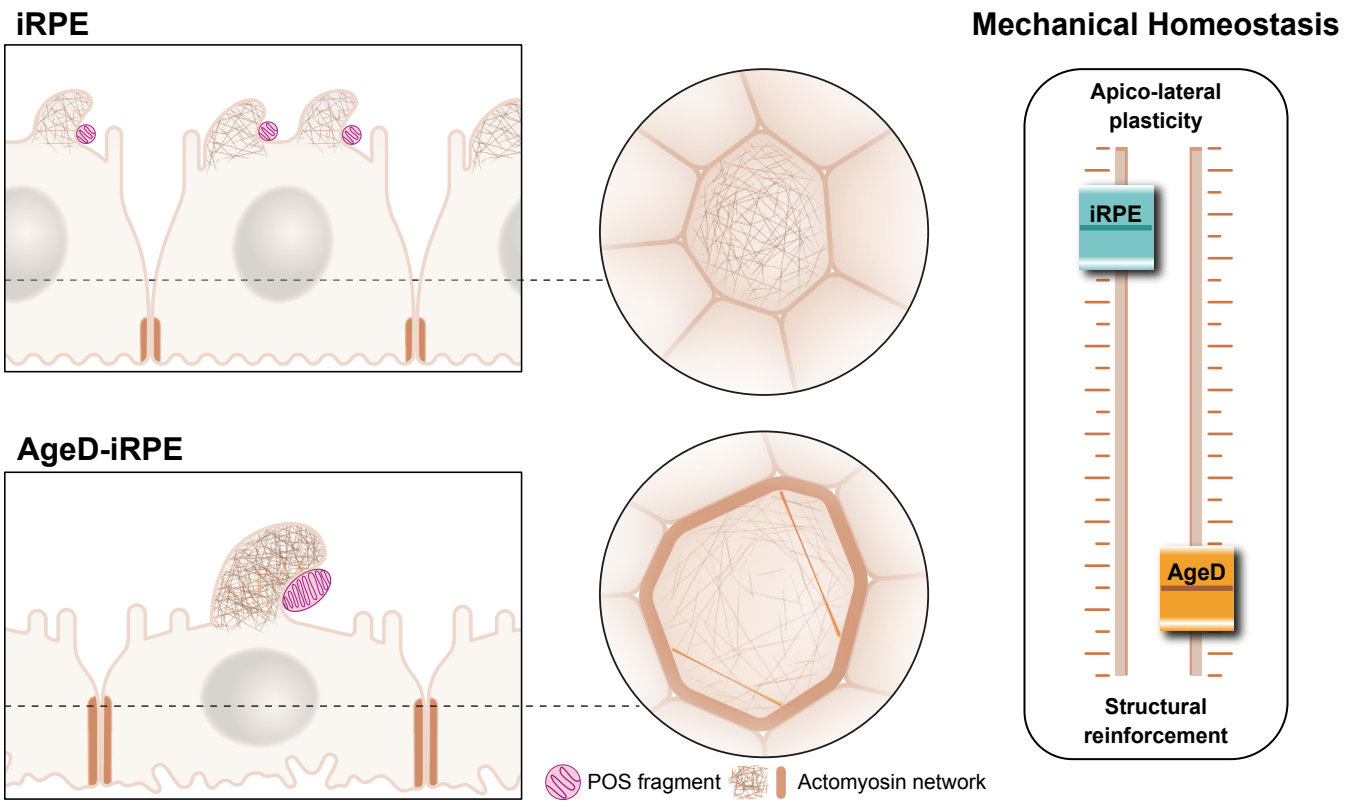
iRPE
AgeD-iRPE
Mechanical Homeostasis
Apico-lateral plasticity
iRPE
AgeD
Structural reinforcement
POS fragment
Actomyosin network